Development of a Dielectrophoretic Chip

for Single Cell Electrorotation

by

Iniyan Soundappa Elango

A Thesis Presented in Partial Fulfillment
of the Requirements for the Degree
Master of Science

Approved April 2012 by the
Graduate Supervisory Committee:

Professor Deirdre R. Meldrum, Chair
Professor Jennifer Blain Christen
Dr. Roger H. Johnson

ARIZONA STATE UNIVERSITY

May 2012

ABSTRACT

Due to heterogeneity at the cellular level, single cell analysis (SCA) has become a necessity to study cellomics for the early detection of diseases like cancer. Development of single cell manipulation systems is very critical for performing SCA. In this thesis, electrorotation (ROT) chips to trap and rotate single cells using electrokinetic forces have been developed. The ROT chip mainly consists of a set of closely spaced metal electrodes (60µm interspacing between opposite electrodes) that forms a closed electric field cage (electrocage) when driven with high frequency AC voltages. Cells were flowed through a microchannel to the electrocage where they could be precisely trapped, levitated and rotated in 3-D along the axis of interest. The dielectrophoresis based ROT chip design and relevant electrokinetic effects have been simulated using COMSOL 3.4 to optimize the design parameters. Also, various semiconductor technology fabrication process steps have been developed and optimized for better yield and repeatability in the manufacture of the ROT chip. The ROT chip thus fabricated was used to characterize rotation of single cells with respect to the control parameters namely excitation voltage, frequency and cell line. The longevity of cell rotation under electric fields has been probed. Also, the Joule heating inside the ROT chip due to applied voltage has been characterized to know the thermal stress on the cells. The major advantages of the ROT chip developed are precise electrorotation of cells, simple design and straight forward fabrication process.

i

TABLE OF CONTENTS

CHAPTER

CHAPTER

LIST OF TABLES

LIST OF FIGURES

Figure

Figure

Figure

Chapter 1

Introduction to cell manipulation using electrokinetic effects

1.1. Introduction

Heterogeneity in terms of gene, protein and metabolites expression at the cellular level has made single cell analysis (SCA) a necessity to study cellomics with cellular specificity. New emerging technologies have enabled SCA, opening the door for better understanding of biological phenomena at the cellular level and earlier disease detection (Wang and Bodovitz 2010). Cancer is the focal point of many efforts as its prevalence has persisted regardless of the technological advances. SCA has proven vital for studying tumor formation and progression in cancer since it is a heterogeneous disease (Wang and Bodovitz 2010).

Even though the complexity behind cancer is yet to be solved, quantification of structural changes at single cell level using SCA can be very useful in developing robust biosignatures for early detection of the disease (Nandakumar et al. 2011). As SCA is critical for the above reasons, it is important to explore the techniques that are commonly used for single cell manipulation, which is elemental in performing SCA.

Several different techniques have been established for particle/cell manipulation, mainly: optical, hydrodynamic, dielectrophoretic, magnetic, and acoustic manipulation techniques. Each technique makes use of different properties of the particle/cell and offers different trapping resolution as shown in Table 1 below (Nilsson et al. 2009). Of these techniques, dielectrophoresis

(electrokinetic phenomenon) based manipulation of cells is of particular interest owing to the various advantages it offers.

In Table 1 , D is the particle/cell diameter, n is the refractive index of the particle/cell, ε is the permittivity of particle/cell and medium, σ is the conductivity of particle/cell and medium, χ is the permeability of the particle/cell, ρ is density of the particle/cell, β is the compressibility of the particle/cell.

Table 1. Comparison of particle/cell manipulation techniques

Manipulation technique	Critical Properties	Buffer demands	Trapping resolution	Trapping force(pN)
Hydrodynamic	D	-	Low(~10μm)	NA
Optical	D, n	Transparent	High(~50nm)	100-2000
Dielectrophoretic	D, ε, σ	pH, Ion, clean surfaces	Medium(~1μm)	200-400
Magnetic	D, χ	-	Medium(~1μm)	2-1000
Acoustic	D, ρ, β	-	Low(~100μm)	100-400

The term "Dielectrophoresis" was coined by H. A. Pohl in 1951 who conducted the early experiments that defined the phenomenon. Recently, dielectrophoresis has become very important due its potential application in micro/nano manipulation (Arnold and Zimmermann 1988). Dielectrophoresis (DEP) is a phenomenon where the presence of a non-uniform electric field in the vicinity of a dielectric particle results in a force exerted on the particle. DEP does not require that the particle be charged; while the magnitude and direction of the force itself has a profound dependence on the properties of the particle and the medium surrounding the particle (Jones 1995).

1.2. Background literature

The advantages of DEP has been utilized in several applications including sorting cells based on size, type and other properties, trapping and rotating individual cells for optical imaging and concentrating cells for bulk manipulation(Fiedler et al. 1998; Andersson and van den Berg 2003; Zahn 2009, pg 133-181). Several of these applications and the appropriate dielectrophoretic systems used are mentioned in this section.

Filtering of particles/cells based on size and properties using dielectrophoresis is one of the most common applications. This is typically done with interdigitated electrode arrays with sets of energized and grounded electrodes. The dielectrophoretic effects have been used to accumulate particles/cells of interest along the electrodes against a fluid flow while other unwanted particles/cells were carried away (Zahn 2009, pg 133-181). Interdigitated electrodes with castellation have been used for positioning, separation as well as concentrating particles/cells (Green and Morgan 1997; Muller et al. 1999; Sebastian, Buckle, and Markx 2006). Another application of dielectrophoresis is sorting particles/cells (An et al. 2009; Fiedler et al. 1998). Travelling wave dielectrophoresis phenomenon, which is achieved with spatially varying phase of electric fields, has been used for levitation, controlled transverse motion and separation of particles/cells (Cui and Morgan 2000; Morgan et al. 1997). Lapizco-Encinas et al. have used insulative dielectrophoresis (iDEP) for selective separation of particles/cells. The main advantages of iDEP method is the isolation of the driving electrodes from the particle, reducing Joule heating and

3

any contamination due to the exposed electrodes (Shafiee et al. 2009). However, iDEP systems use high applied voltages (> 100V) and low frequencies, which limit the precision of control on a single particle/cell basis (Lapizco-Encinas et al. 2004, 2004).

Particles/cells trapping using quadrupole (4 electrodes), octupole (8 electrodes) and addressable dot traps have been demonstrated. Typically trapping of one or a few particles/cells is useful for close monitoring and manipulation. In this case, the system consists of electrodes which create a static or rotating electric field forming an electrocage that enables both trapping and trapping with rotation (ROT) of particles/cells (Muller et al. 1999; Taff and Voldman 2005; Voldman 2006; Schnelle, Muller, and Fuhr 2000).

The main aim of this project is single cell manipulation using electrorotation (ROT). Fuhr et al. have completed extensive studies on electrorotation of cells/microbeads. The behavior of a single biological cell in a rotating electric field was investigated both theoretically and experimentally by calculating the torque and forces dependent on the electrical properties of the cell (Fuhr and Kuzmin 1986; Schnelle et al. 1993). Adhering animal cells were cultured under permanent electric field application to probe the effects on cell growth and were claimed to be insignificant (Fuhr et al. 1994). The degree of electropermeabilization of the plasma membrane of mammalian cells has been correlated to cell medium conductivity, by measuring the temporal and spatial intake of propidium iodide stain (Djuzenova et al. 1996). Dielectrophoresis based electrode elements capable of funneling, aligning, caging, and switching were

4

designed for focusing, trapping and separating cells and microbeads (Muller et al. 1999). Cell division rates, cell motility and viability were probed to find that field application is limited by dielectric breakdown of cells at low frequency and Joule heating at high frequencies (Glasser and Fuhr 1998). Fuhr et al. has also shown experimentally that a dipole approximation for particles/cells in evaluating the dielectrophoretic forces can be a good estimate only for particles/cells that is quarter the size of the electrocage and for larger particles higher order quadrupole approximation is necessary (Schnelle et al. 1999). A combination of dielectrophoretic and laser trapping (electro-optical trap) for electrorotation which offers the advantage of low field operation has been demonstrated (Schnelle et al. 2000).

1.3 Theory

Every particle has electrical properties which are defined by its electrical conductivity, permittivity, shape and size. The conductivity and permittivity are material dependent parameters. Depending upon how a particle responds to an applied electric field, it can be classified into a conductor, dielectric or a lossy dielectric. A perfect conductor will aid in transport of charges (e.g. electron, ion) in the direction of the electric field making the electric potential distribution uniform across it. Whereas, a perfect dielectric has immobile charges (e.g. electron, ion) which results in polarization with no current flow and a potential distribution that is governed by Gauss's law. Lastly, in case of a lossy dielectric, there will be polarization as well as non-negligible conduction current. In reality, every particle will exhibit both conduction and polarization to a finite extent

5

(Zahn 2009, pg 133-181). Thus a particle, when subjected to an electric field, has charge distributions in and around it determined by its electrical properties. As a result, the particle may experience forces and/or torques due to the electric field which forms the basis of electrokinetics.

Electrokinetics is a broad classification of a set of phenomena that occurs in a heterogeneous fluid containing particles in the presence of an electric field. Typically, the effects of electrokinetic phenomena are dominant in particle sizes roughly above 1µm and below 1mm. Beyond these limits, smaller particles are more influenced by Brownian and van der Waals forces and larger particles are more influenced by gravitational forces (Jones 1995). As an illustrative example, consider an aqueous medium that has mobile ions and charged particles of the described size. In this case, the local concentration of the mobile counter-ions near the surface of the charged particles will be higher forming an interfacial double layer of charges. Now, in presence of an external electric field, there is a force exerted on the mobile charge layer (diffuse layer), generating a tangential motion of the mobile charge, dragging along the medium with respect to the particle (α-dispersion phenomenon, frequency up to 1 kHz). The particle itself will experience a force under the influence of the electric field due to its charge (Jones 1995). Depending upon the type of relative motion that occurs between a surface/particle and mobile ions in a medium, several different electrokinetic phenomena are observed. Dielectrophoresis, electroosmosis, and Joule heating are of particular interest in studying the effects of electric field on biological cells (Oh et al. 2009).

6

Dielectrophoresis is the motion of a dielectric particle caused by non-uniformity in an electric field. Electroosmosis is the motion of the medium along with diffuse layer of charges relative to a stationary surface with a changing electric field (e.g. electrode). Joule heating (Ohmic heating) is the heating of a material due to flow of charges through the material. It is to be noted that DEP is an effect that is directly dependent on the interaction of a particle with electric field, whereas electroosmosis and Joule heating are hydrodynamic effects that depend upon the interaction of the heterogeneous medium with the electric field (Oh et al. 2009).

1.3.1 Dielectrophoresis

A dielectric particle, like a biological cell, when subjected to a non-uniform electric field, experiences a DEP force that is be determined by the size, shape and complex permittivity of the particle and surrounding medium as well as the frequency, strength and non-uniformity of the localized electric field. The cell has a net negative surface charge in the order of $10mC/m^2$ which results in an electrical double layer around the cell. But, the movement of massive diffuse layer ions is slow and this type of polarization is effective only in low frequency ranges (α-dispersion phenomenon, frequency up to 1 kHz). The DEP force is a resultant of polarization along the interface (e.g. cell membrane) between two materials with different complex permittivities (e.g. cell cytoplasm and cell medium). The polarization (Maxwell-Wagner interfacial polarization, β-dispersion phenomenon, frequency range - 1 kHz- 100 MHz) results from collection of charge along the interface which can be approximated as a dipole

7

bound to the particle. The non-uniform external electric field exerts a Columbic force on the dipole. This necessitates that the non-uniformity of the local electric field should be on the order of the size of the particle and materials have different complex permittivities. Dielectrophoresis should not be confused with electrophoresis which is a closely related electrokinetic phenomenon that occurs only when a charged particle is exposed to an electric field. In case of electrophoresis, the electric field is always uniform and the inherent charge of the particle is responsible for the Columbic interactions between the field and the particle (Jones 1995; Heida 2003). Figure 1a shows the difference between electrophoresis and dielectrophoresis. Figure 1b shows the behavior of a dielectric particle in presence of a non-uniform electric field (Sung 2007).
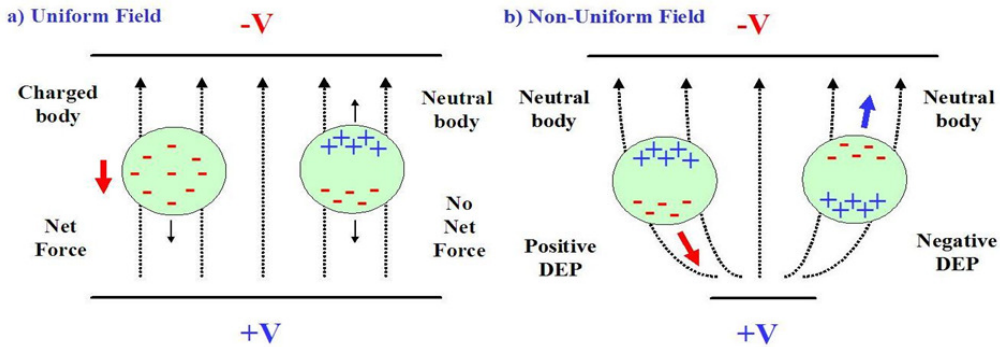
Figure 1. Dielectrophoresis principle

The time averaged DEP force using a dipole approximation acting on an isolated sphere suspended in infinite medium is given by the following equation (Jones 1995, pg 34-61):

$$<\vec{F}_{DEP}> = 2\pi \in_m R^3 * Re(f_{CM}) * \vec{\nabla} E^2_{rms} \quad \text{where} \quad f_{CM} = \frac{\overline{\in}_p - \overline{\in}_m}{\overline{\in}_p + 2\overline{\in}_m} \quad \text{and} \quad \overline{\in} = \in -\frac{i\sigma}{\omega}$$

8

In the above equation, R is the radius of the suspended sphere, $Re(f_{CM})$ is the real part of the Clausius-Mossotti factor, f_{CM} is the Clausius-Mossotti factor, $\bar{\epsilon}$ is the complex permittivity, ϵ is the dielectric permittivity, σ is the conductivity, ω is the angular frequency of the applied electric field and $\vec{\nabla}E^2_{rms}$ is the gradient of the root mean square of the applied electric field. The suffix m stands for medium and p for particle.

From the time averaged dipole approximated DEP force equation, it can be observed that the force is directly proportional to the cube of the radius of the sphere, the real part of the Clausius-Mossotti factor that varies between $1(\bar{\epsilon}_p \rightarrow \infty$) and -0.5 ($\bar{\epsilon}_m \rightarrow \infty$) which determines the direction of the force and the gradient of the mean square of the applied electric field. Depending upon the polarity of the DEP force acting on a particle it can be classified into positive DEP and negative DEP forces. The positive DEP force attracts the particle towards the higher electric field gradient and negative DEP force repels the particle from high electric field gradient as shown in Figure 1b. In case of biological cells, to minimize the negative effects that may occur in presence of high electric field gradients, it is preferred to operate in negative DEP regime which is controlled by making the real part of the complex permittivity of medium higher than that of the cells.

In the above DEP force equation, the effect of spatial change of phase of the electric field has not been taken into account. When the phase of the electric field varies spatially, two different types of dielectrophoretic forces are observed

depending upon the arrangement of electrodes, namely travelling wave dielectrophoresis (TWDEP) and electrorotation (ROT).

1.3.1.1 Travelling wave dielectrophoresis

Travelling wave dielectrophoresis is a phenomenon that occurs when the applied electric field has spatially varying phase as shown in Figure 2. The F_{DEP} equation for a spatially varying electric field is given below.

$$\vec{E}(\vec{r},t) = Re[(\vec{E}^{re}(\vec{r}) + i\vec{E}^{im}(\vec{r}))\exp[i\omega t]]$$

$$<\vec{F}_{DEP}> = 2\pi \in_m R^3 * Re(f_{CM}) * \vec{\nabla}E^2_{rms} - 2\pi \in_m R^3 Im(f_{CM})\nabla \times Re[\vec{E}] \times Im[\vec{E}]$$

The time averaged dielectrophoretic force has a travelling wave component defined by the second term in the equation(Schnelle, Muller, and Fuhr 2000). It has to be noted that the TWDEP component is proportional to the imaginary part of the Clausius-Mossotti factor and to the cube of the radius of the sphere. The TWDEP force mainly finds its application in smooth conveyance of particles that are levitated from the surface. Particle rotation may be observed in the direction of movement as shown in Figure 2.
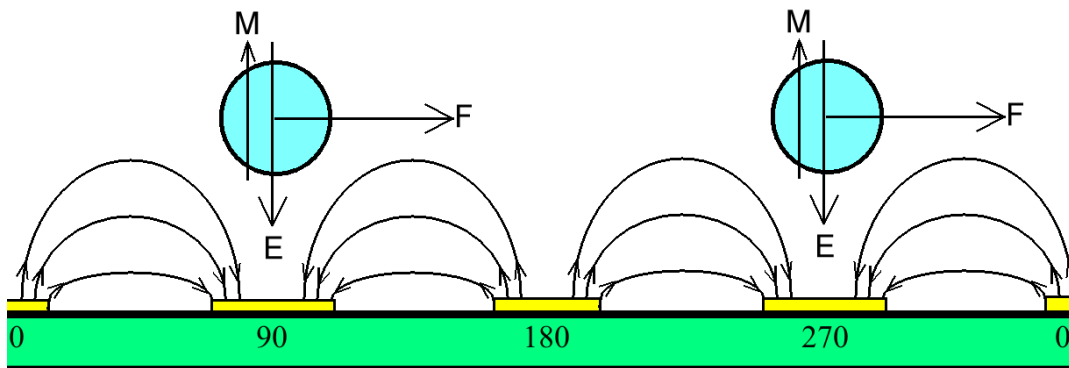
Figure 2. Travelling wave dielectrophoresis principle

1.3.1.2 Electrorotation

Electrorotation occurs when the particle is in the presence of a rotating electric field as shown in Figure 3. The time averaged dipole approximated torque exerted by a rotating electric field is given by the following equation (Schnelle, Muller, and Fuhr 2000).

$$< \vec{N} >= 4\pi \in_m R^3 Im(f_{CM}) Re[\vec{E}] \times Im[\vec{E}]$$
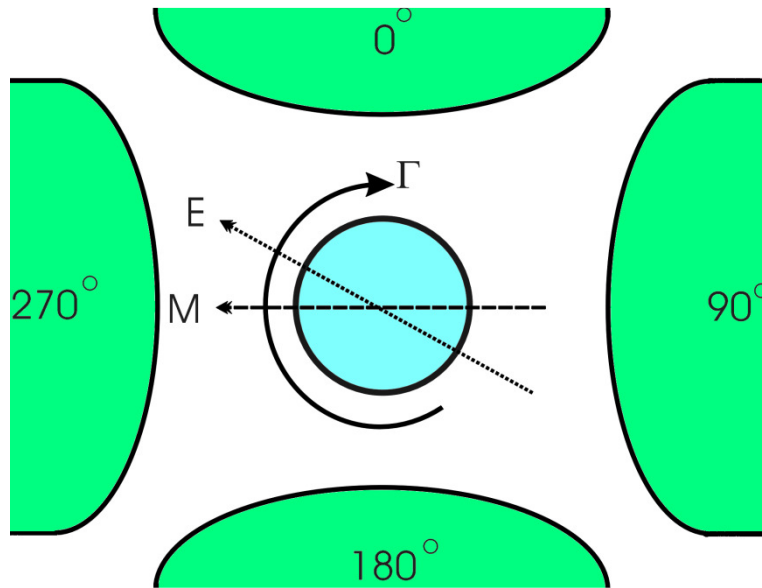
Figure 3. Electrorotation principle

Again it is seen that the electrorotation of a particle depends upon the imaginary part of the Clausius-Mossotti factor and the mean square of the electric field unlike the DEP force which is proportional to the gradient of the mean square electric field.

All the force equations so far described are valid under the assumptions that the particle considered is spherical and can be approximated as a dipole. Also, the in-homogeneity of the applied electric field should be in the order of the particle size that is manipulated. Under specific circumstances, it may be necessary to

consider higher order moment approximations to accurately predict dielectrophoretic forces.

1.3.1.3 Higher order moment approximation

As discussed previously a cell in presence of an electric field can be approximated as a multipole whose order depends upon the level of accuracy with which the DEP force acting on the cell has to be determined. Shown below in Figure 4 is the multipole scheme that can be derived from a point charge separated by appropriate vectors. In the figure, n denotes the order of the multipoles (n=0 for monopole, n=1 for dipole, n=2 for quadrupole and n=3 for octupole) generated by placing two multipoles of order n-1 opposite to each other, separated by a distance vector. While the dipole approximation for a cell holds for most of the observed DEP effects, there are few exceptional cases when higher order approximations are required. When a cell is at or near a field null as in case of the center of an octode electrocage during electrorotation or the cell is placed in a very highly non-uniform electric field where the polarization is more complex than a dipole. The multipole approximations are required to accurately predict the behavior of cells in such situations (Washizu and Jones 1994; Schnelle et al. 1999).
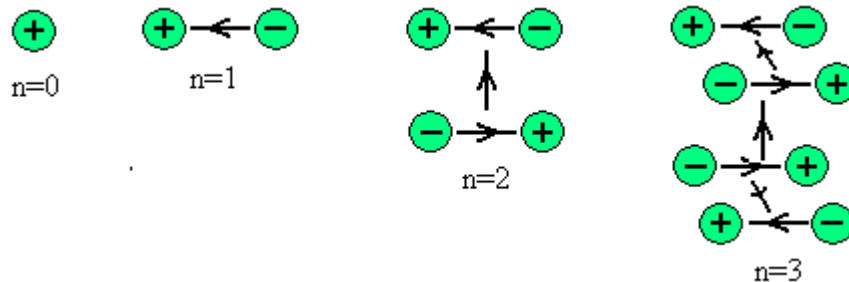
Figure 4. Representation of multipoles using point charge model

12

In order to predict the DEP force that acts on a cell using multipole approximations, Jones and Washizu have formulated the higher order DEP force terms as derivatives of electromechanical potentials (U) as shown in the below equations (Washizu and Jones 1994).

$$\vec{F}_{DEP} = -\nabla(U_1 + U_2 + U_3 + ..) \text{ where,}$$

$$U_1 = -2\pi R^3 \in_m \left(\frac{\in_p - \in_m}{\in_p + 2\in_m} \right) \left[\left(\frac{\partial \varphi_{ext}}{\partial x} \right)^2 + \left(\frac{\partial \varphi_{ext}}{\partial y} \right)^2 + \left(\frac{\partial \varphi_{ext}}{\partial z} \right)^2 \right]$$

$$U_2 = -\frac{4\pi R^5 \in_m}{3} \left(\frac{\in_p - \in_m}{2\in_p + 3\in_m} \right) \left\{ \begin{array}{l} \frac{1}{2} \left[\left(\frac{\partial^2 \varphi_{ext}}{\partial x^2} \right)^2 + \left(\frac{\partial^2 \varphi_{ext}}{\partial y^2} \right)^2 + \left(\frac{\partial^2 \varphi_{ext}}{\partial z^2} \right)^2 \right] \\ + \left(\frac{\partial^2 \varphi_{ext}}{\partial y \partial z} \right)^2 + \left(\frac{\partial^2 \varphi_{ext}}{\partial z \partial x} \right)^2 + \left(\frac{\partial^2 \varphi_{ext}}{\partial x \partial y} \right)^2 \end{array} \right\}$$

$$U_3 = -\frac{2\pi R^7 \in_m}{5} \left(\frac{\in_p - \in_m}{3\in_p + 4\in_m} \right) \left\{ \begin{array}{l} \frac{1}{6} \left[\left(\frac{\partial^3 \varphi_{ext}}{\partial x^3} \right)^2 + \left(\frac{\partial^3 \varphi_{ext}}{\partial y^3} \right)^2 + \left(\frac{\partial^3 \varphi_{ext}}{\partial z^3} \right)^2 \right] \\ + \frac{1}{2} \left[\begin{array}{l} \left(\frac{\partial^3 \varphi_{ext}}{\partial x^2 \partial y} \right)^2 + \left(\frac{\partial^3 \varphi_{ext}}{\partial x^2 \partial z} \right)^2 + \left(\frac{\partial^3 \varphi_{ext}}{\partial y^2 \partial x} \right)^2 \\ + \left(\frac{\partial^3 \varphi_{ext}}{\partial y^2 \partial z} \right)^2 + \left(\frac{\partial^3 \varphi_{ext}}{\partial z^2 \partial x} \right)^2 + \left(\frac{\partial^3 \varphi_{ext}}{\partial z^2 \partial y} \right)^2 \end{array} \right] \\ + \left(\frac{\partial^3 \varphi_{ext}}{\partial x \partial y \partial z} \right)^2 \end{array} \right\}$$

In the above equation, φ_{ext} is the net electrostatic potential at a point and the other terms are the same as in the dipole approximation.

1.3.2 Electroosmosis

In the DEP chip used for cell handling, electroosmosis is observed near the surface of the electrodes. In electroosmosis, the mobile ions in the cell

medium form a counter-ion diffuse layer near the electrodes resulting in an electrical double layer. In certain cases where the electrodes are in close proximity, there will be a tangential component of the electric field between those electrodes which will drive the mobile ions in the diffuse layer laterally dragging the medium. This may result in a rotational fluid motion near the electrodes. The equation for the electroosmotic velocity is shown below (Oh et al. 2009).

$$< V_{ACEO} >= \left(\frac{\in_m \varphi_0^2 \Omega^2}{8\eta d(1+\Omega^2)^2} \right) \qquad \text{where,} \; \Omega = \frac{1}{2}\pi kd \left(\frac{\in_m}{\sigma_m} \right) \omega$$

In the above equation, $\in_m$ is the dielectric permittivity of the medium, φ_0 is the initial potential, Ω is the non-dimensional frequency as defined by the equation, k is the inverse of the Debye length, σ_m is the conductivity of the medium, η is the dynamic viscosity of the medium and d is the cross-sectional position starting from the center of the gap between the electrodes.

From the electroosmotic velocity equation, it can be observed that the velocity approaches zero at very low and high frequencies. Also, the electroosmotic effect becomes negligible with increase in the medium conductivity. The DEP chip is designed to operate in frequencies greater than 500 kHz and medium conductivity on the order of 1-10 S/m where the electroosmotic effect has to be probed.

1.3.3 Joule heating

Joule heating is an effect observed when the moving charged particles (electrons in metals and ions in medium) that comprise electrical current collide with stationary atoms resulting in energy transfer that manifests itself as heat.

14

This heating effect results in gradients in the conductivity and permittivity of the medium. The electric field interacts with the gradients, resulting in fluid motion that may drag the particles suspended in the medium.

If the rate of change of the conductivity and the permittivity is known as a function of temperature, it is possible to evaluate the time averaged electrothermal (ET) hydrodynamic force induced by electric field due to the gradients in the conductivity and permittivity of the medium (Oh et al. 2009).

$k\nabla^2 T + \sigma_m E^2 = 0$ where, k is the thermal conductivity of the medium

σ_m is the conductivity of the medium

$$< \vec{F}_{ET} >= 0.5 \in_m \nabla T \vec{E}^2 \Pi(\omega) \text{ where } \Pi(\omega) = \left(\frac{\alpha - \beta}{1 + (\omega\tau)^2} - \frac{\alpha}{2} \right)$$

$$\alpha = (1/\in_m)(\nabla \in_m /\nabla T),$$

$$\beta = (1/\sigma_m)(\nabla\sigma_m /\nabla T), \tau = \in_m /\sigma_m$$

In the above equation, α is the percentage change of medium permittivity per Kelvin, β is the percentage change of medium conductivity per Kelvin, $\Pi(\omega)$ is a unit-less function of frequency and τ is the charge relaxation time constant.

It is shown that the temperature change is proportional to the electrical conductivity of the medium. Therefore lower medium conductivity eliminates current flow and there by joule heating. The electrothermal hydrodynamic force is directly proportional to the temperature gradient and the square of the magnitude of the electric field. Both the temperature gradient and the electric field are

15

proportional to the applied voltage. As such, the voltage affects the force significantly. It can also be noted that the force is inversely proportional to the frequency. High frequency operation therefore can be used to reduce Joule heating effects.

1.4 Electrorotation chip overview

The main focus of this thesis is to develop an electrorotation chip, which will aid in single cell imaging aimed at early detection of diseases. The electrorotation (ROT) chip consists of a set of deposited metal electrodes on two substrates, which are bonded with a polymer spacing layer between the substrates. The electrodes are exposed at the center of a microchannel formed by the polymer layer. This microchannel guides cells suspended in cell medium to the center of the electrocage. The electrodes form an electric field cage (electrocage) that can trap and rotate cells when stimulated with a high frequency AC voltage with appropriate phase shift. Figure 5 shows the 3-D arrangement of the electrodes forming an electrocage.
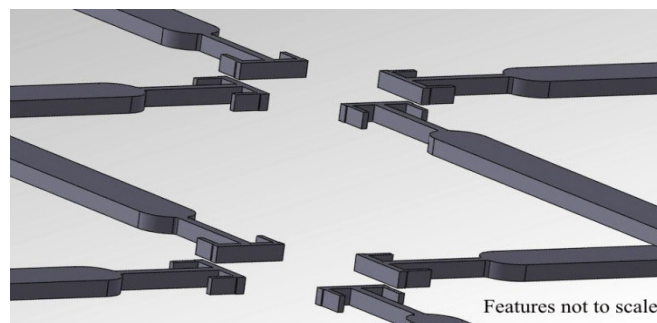
Figure 5. 3-D electrode arrangement in ROT chip

1.5 Discussion

It is evident that several electrokinetic phenomena occur in the presence of alternating electric fields. For cell manipulation applications, it is critical to understand the various electrokinetic phenomena and parameters that affect them. The most critical phenomena to be considered are dielectrophoresis, electroosmosis and Joule heating for electrorotation of cells. The F_{DEP} force and ROT torque are the two types of dielectrophoretic forces that determine cell electrorotation in the ROT chip. Whereas, Joule heating is undesired as an increase in the temperature can stress the cells. The ROT chip design has been considering the above mentioned electrokinetic phenomena for cell electrorotation.

Chapter 2

Design selection for electrorotation chip

The design and dimensions of the electrodes determine the dielectrophoretic guiding, trapping and rotating forces acting on a cell, the amount of Joule heating and the ability to repel other cells from entering the electrocage. The initial electrode design guidelines for the ROT chip were adopted from Fuhr et al. (Fuhr et al. 2003). COMSOL Multiphysics was used to simulate the electric field distribution, suitable phase configuration and probe Joule heating in the electrocage. Further, several design iterations have been carried out to improve the fabrication yield and ROT control.

2.1 Initial ROT chip designs

The electrode design for the ROT chip consisted of three regions namely a) head region, b) feed region and c) contact region. The head region of the electrode forms the cage, the contact region is used for electrical interfacing and the feed region connects the head and the contact regions. The head region design should be optimized to create highly inhomogeneous electric fields to increase the DEP force for good trapping in the cage and repel nearby cells from entering into the cage due to external forces like thermal convection or fluid drag force. The feed region should be smaller in width near the head region to minimize the thermal convection towards the electrode cage (Fuhr et al. 2003). Following the above guidelines, a myriad of electrode designs are possible which can make a ROT chip. But, only prevalently used electrode shapes have been simulated and

18

fabricated for better trapping, rotation of trapped cell and repelling of cells outside the electrocage. The feed region width was optimized for high fabrication yield and minimal thermal convection.

Four iterations of the electrode designs were fabricated with modifications to improve the fabrication yield. In design iteration 1, electrodes with three different head shapes were fabricated which included 1) Flat head 2) Semi-elliptical head and 3) Arrow head with two different interspacing (between opposite electrodes of same plane) 60µm and 120 µm as shown in Figure 6. Due to excessive etching of the deposited metal underneath the mask region (with aqua regia etchant), the electrodes were under-dimensioned leading to low yield. However, quadrupole electrodes were used to demonstrate planar cell rotation (about the z-axis) by stimulating the electrodes with voltages that had phase shift of 90° forming a planar rotating electric field. Owing to the poor yield in design iteration 1, the design iteration 2 had only flat head electrodes with interspacing 120 µm. The feed and head regions were scaled up by around 40% and 20% respectively to increase the yield. The challenge with metal etching was addressed by using a commercially available etchant (TFA etchant). With this design, 3-D rotation of latex beads and K562 leukemia cancer cells were demonstrated. The 120µm interspaced electrodes were separated by 120 µm spacing layer in order to have a symmetrical rotating field. This implies that the cell was levitated to 60µm above the bottom substrate, which is problematic because the height that the cell can be levitated is limited by the working distance of the objectives used for imaging. As such, it is desired to have the cell as close as possible to the bottom

19

substrate. Thus in design iteration 3, the same flat electrode geometry with three different interspaces of 50µm, 60µm and 80µm were fabricated. While all three interspacing electrodes precisely rotated cells, 60 µm was chosen as the standard interspacing for future designs considering the ease in fabricating the spacing layer (one step photolithography), proximity of the levitated cell to the bottom substrate (30µm), minimal microchannel clogging during the bonding process (diffuse bonding technique) and the design rules for electrode dimensions (Fuhr et al. 2003) (Note: Please refer to Chapter 3 for more details on fabrication processes). In design iteration 4, the form factor of the ROT chip was modified for compatibility with a proprietary imaging platform retaining the flat head electrode design with 60 µm interspacing. In the first three design iterations, the fluidic connections were made with Nanoport assemblies (Upchurch Scientific, Oak Harbor, WA) and electrical connections using soldered wires. While in design iteration 4, AS568A silicone o-ring face seals (McMaster-Carr, Santa Fe Springs, CA) were used for fluidic connection with ports cut on the face of the chip. Pogo pins (Mouser electronics, Mansfield, TX) were used to make electrical contact with the exposed bond pads.
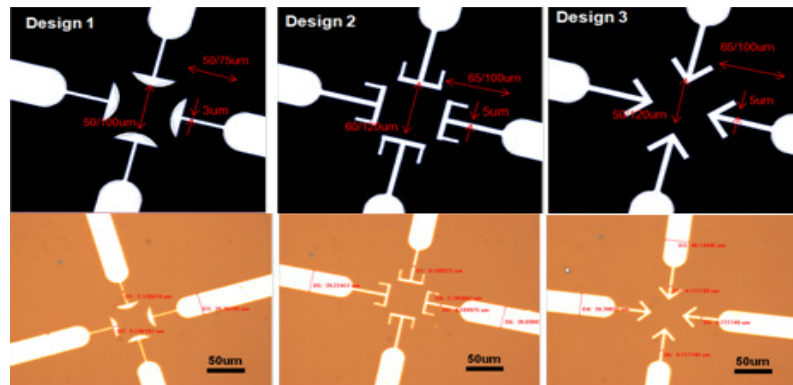
Figure 6. Electrode designs of design iteration 1

20

2.2 Electrorotation chip simulation

2.2.1 Electrode design simulation

　　Various electrode designs were simulated using COMSOL 3.4 to optimize the electrode shape and dimensions for maximum cell trapping and rotation control for a given voltage. From the DEP force equation, it can be observed that the effect of the shape of electrodes is reflected in the $\vec{\nabla}E^2_{rms}$ term. So, in order to optimize the electrode shape for maximum trapping and rotation, the electric field distribution and its gradient were analyzed.

　　Laplace equation for electrostatics was used to simulate the effect of applying a voltage to a medium using the electrodes. The conductivity of the medium and charge distribution density was assumed to be zero. The model yielded convincing results for the electric field distribution pattern. The Laplace equation for electrostatics is derived from the Gauss's law in derivative form. The Laplace equation is given below,

$$\nabla^2\varphi = 0 \quad \text{where } \varphi \text{ is the electrostatic potential}$$

　　The electrode shapes typically used for ROT application are semi-elliptical, arrow and rounded arrow (Maswiwat, Holtappels, and Gimsa 2006; Reichle et al. 1999). In this thesis, the simulation of the electrode shapes were limited to semielliptical, arrow and concave head shapes. All the designs were simulated using a 2-D model. Quadrupole and octupole head electrode designs with 60µm interspacing were simulated with 4V peak-to-peak sinusoidal input of frequency 2MHz and phase shift of 90° (quadrupole) and 45° (octupole) between adjacent electrodes. The relative permittivity of the medium was set to 80.2

21

(permittivity of water in the frequency ranges of interest). Except for the electrodes all the other boundaries were set as distributed capacitance with $V_{ref} = 0$ and ε_r as 80.2 for the boundary condition. With the above stated sub-domain settings and boundary conditions in the electrostatics application mode, the electric field magnitude and its gradient were analyzed to determine the optimum electrode shape.

The electric field magnitude (E_{norm}) is given by the equation below,

$$E_{norm}(t) = \sqrt{\left|E_x(t)\right|^2 + \left|E_y(t)\right|^2 + \left|E_z(t)\right|^2}$$ Where, x, y and z are the Cartesian coordinate axes.

2.2.1.1 Arrow shape

The arrow head shaped electrodes were simulated using a set of 2-D quadrupole and octupole designs, varying the height and keeping the base width constant. The base width of quadrupole electrodes was 45µm and that of octupole electrodes was 21.6µm. The base to height ratio of the electrode head was varied from 6:1 to 6:10 in 10 steps and the results thus obtained were analyzed.

In Figure 7 the norm value of the electric field (E_{norm}) is plotted for only three quadrupole arrow head shaped electrodes at two different time values (t=0 and t=0.125T, where T is the period of the wave). The base width to height ratios (b:h) for each set of electrodes are 6:1, 6:5 and 6:10. The electric field distribution in the electrocage along the line y=0 at t=0s and x=y at t=0.125T s (45° phase shift) for the electrodes have been plotted. It can be observed that the E_{norm} value between the tip of the electrodes at t=0s along y=0 line is maximum near the

22

electrode tips and drops immediately. The huge electric field gradient near the tip implies that there will be a very high DEP force, which will immediately drop towards the center. Considering that the electric field gradient is at a maximum near the electrode tips does not help the stability of the trap. It is to be noted that, with an increase in height of the arrow head, the surface area forming the electrocage reduces since the arrow gets sharper. As a result, trapping at t=0.125T s (phase shift 45°) along x=y line reduces considerably as shown in the figure. In this case, a cell that is initially off the center of the electrocage may not be repelled to the center of the electrocage and stably trapped. This implies that the optimal design should have sufficient area forming the cage, as well as sufficient electric field gradients to stabilize and effectively trap a cell. Comparing b:h::6:1 and b:h::6:10, at t=0s the E_{norm} value at the tip is 4 time greater for the sharper arrow, but at t=0.125T s the E_{norm} value along x=y line is reduced to half the value. Thus, b:h::6:1 is a better design compared to b:h::6:10 as the trapping is better and there is no significant difference in the electric field distribution near the center of the electrocage.

Figure 7. 2-D E_{norm} plot of arrow head shaped quadrupole electrodes at t=0s along y=0 and at t=0.125T s along x=y line.

Figure 8. 2-D E_{norm} plot of arrow head shaped octupole electrodes at t=0s along y=0 and at t=0.125T s along x=y line.

In Figure 8, the E_{norm} distribution is plotted for only 3 octupole arrow head shaped electrodes at two different time values (t=0 and t=0.125T). The base to height ratio was maintained same as the quadrupole electrode design. It can noted that for t=0s along y=0 line and t=0.125T s (45° phase shift) along y=x line have same E_{norm} values as expected. Similar to the quadrupole design, the electric field gradient is at a maximum near the electrode and reduces immediately. The increase in the electrode number improves the trapping stability due to greater trapping forces as shown in Figure 10. Therefore, the octupole electrode design with base width to height ratio of 6:1 was fabricated in design iteration 5 for testing purposes.

Figure 9. Electric potential and field distribution for 2-D quadrupole arrow head shaped electrode design (b:h::6:10) (x, y scale = 10e-4 m)

Figure 10. Electric potential and field distribution for 2-D octupole arrow head shaped electrode design (b:h::6:10) (x, y scale = 10e-4 m)

Figures 9 and 10 show the surface plots of electric potential distribution and 3-D height data determined by the magnitude of the electric field values of the 2-D quadrupole and octupole arrow head electrodes with b:h::6:10 respectively. The height data clearly indicates that octupole electrodes have better trapping than quadrupole electrodes.

2.2.1.2 Semi-elliptical shape

The semi-elliptical shaped electrodes were simulated using a set of 2-D designs keeping one radius (R_a) constant and varying the other radius (R_b). The R_a of quadrupole electrodes was 22.5µm and that of octupole electrodes was 10.8µm. The R_a to radius R_b ratio of the electrode shape was varied from 3:1 to 3:10 and the results obtained were analyzed.

In Figure 11, the E_{norm} distribution is plotted for only three geometries at t=0s along the line y=0 and at t=0.125T s along x=y line. The R_a to R_b ratio

(R_a:$R_{b)}$ for the geometries are 3:1,3:5 and 3:10. Compared to the arrow shaped electrodes, the semi-elliptical electrodes have lower E_{norm} values near the electrode tips. The electric field gradient also varies more uniformly across the electrocage which will enable stable trapping. Also, the area of the electrode which forms electrocage is higher than the arrow electrodes which is supported by the nearly identical E_{norm} values at t=0.125T s along x=y line as shown in Figure 11.
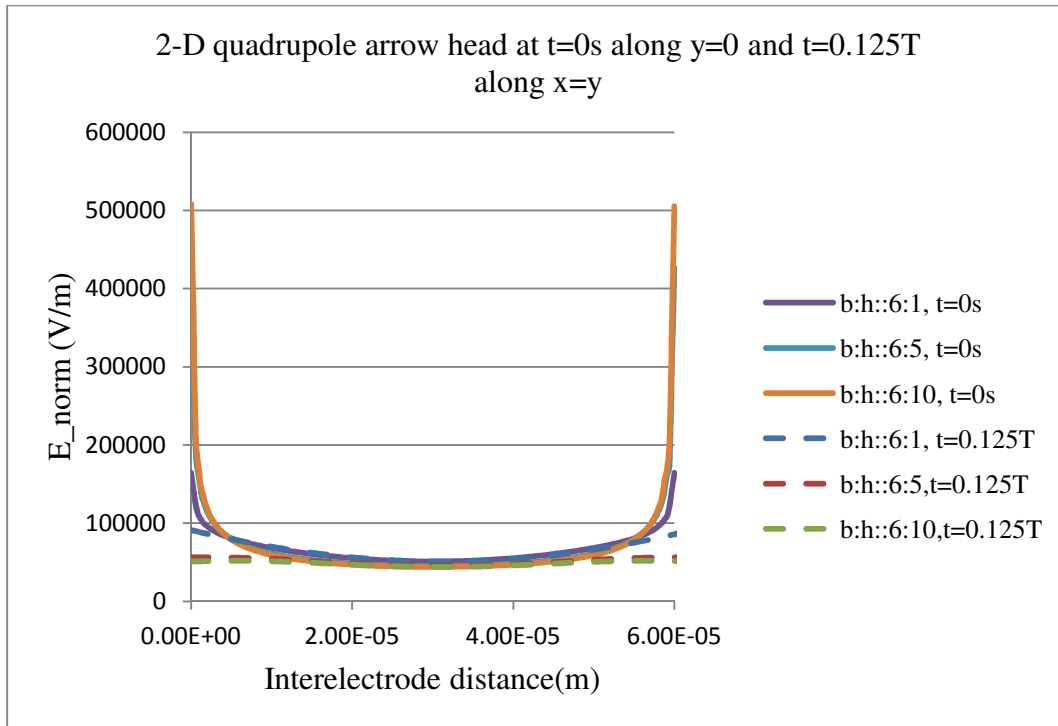

Figure 11. 2-D E_{norm} plot of semi-elliptical head shaped quadrupole electrodes at t=0s along y=0 and at t=0.125T s along x=y line.
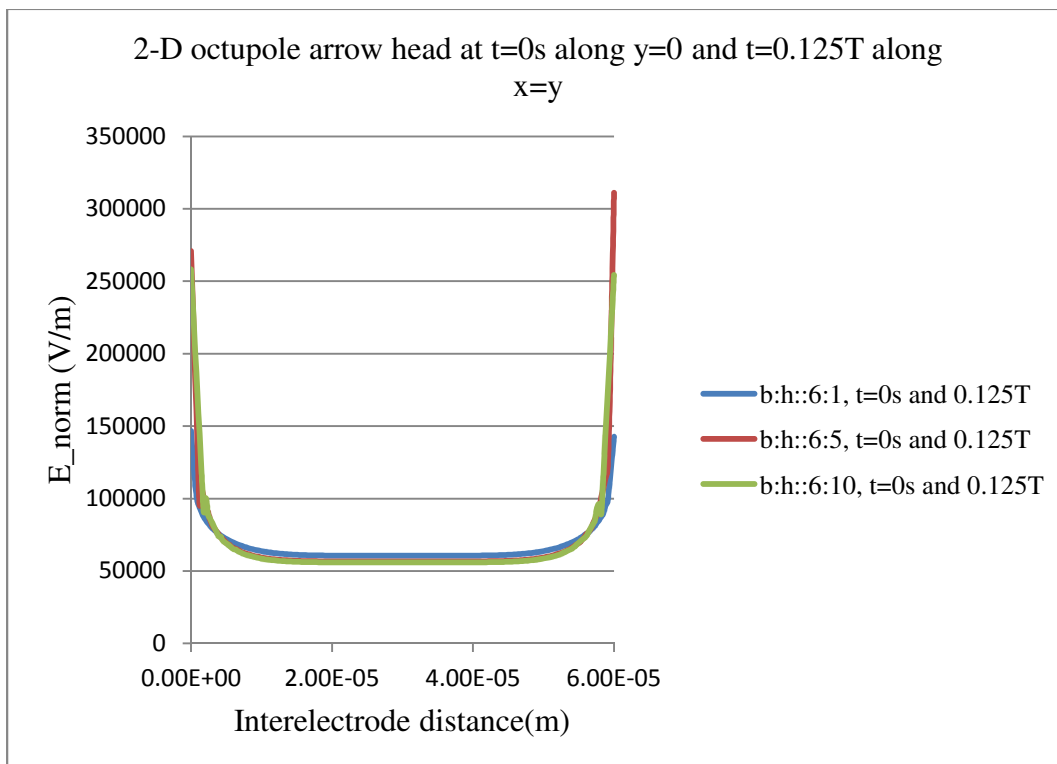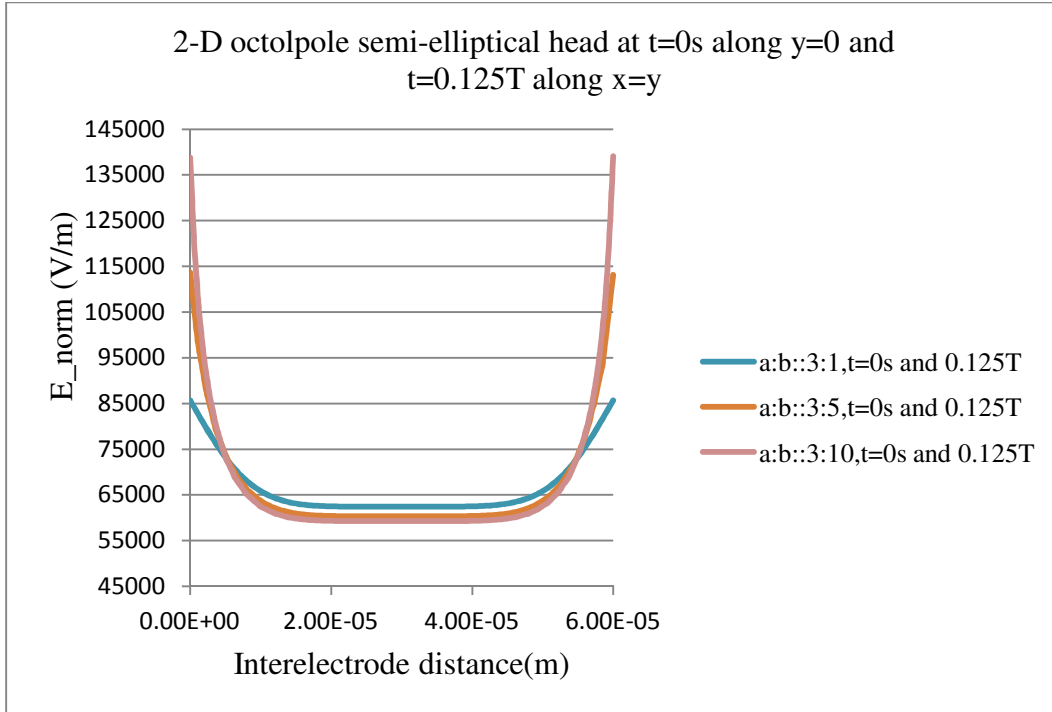
Figure 12. 2-D E$_{norm}$ plot of semi-elliptical head shaped octupole electrodes at t=0s along y=0 and at t=0.125T s along x=y line.

In Figure 12, the E$_{norm}$ distribution is plotted for only three octupole semi-elliptical head shaped electrodes at two different time values (t=0 and t=0.125T). It can noted that for t=0s along y=0 line and t=0.125T s (45° phase shift) along y=x line have same E$_{norm}$ values as expected. Since semi-elliptical electrodes have large area forming the electrocage and a greater number of electrodes, greater trapping stability is possible. A semi-elliptical electrode design with R$_a$ to R$_b$ ratio 3:9 was included in design iteration 5 for testing purposes.
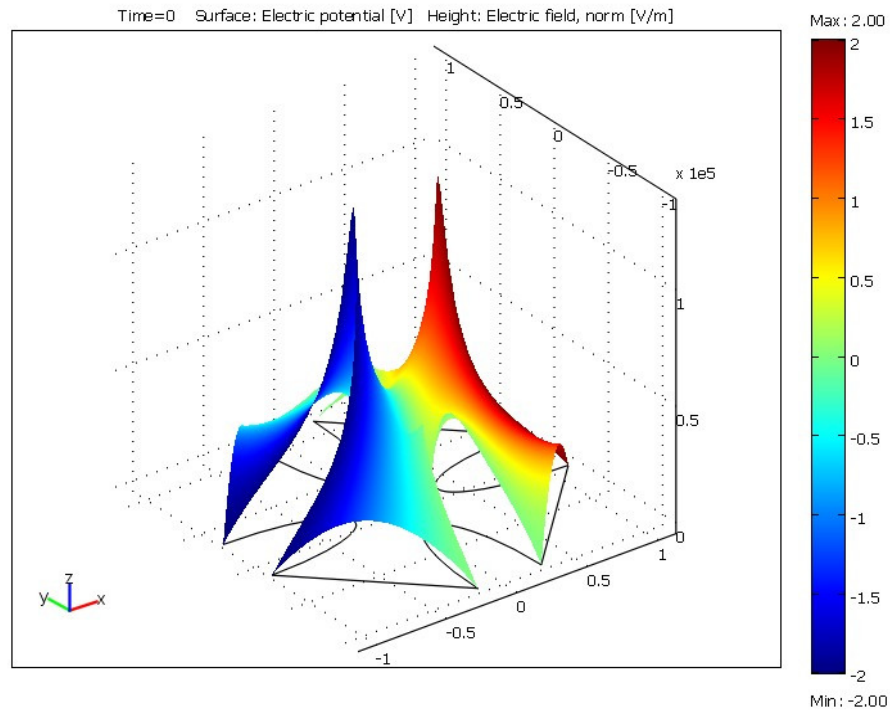
Figure 13. Electric potential and field distribution for 2-D quadrupole semi-elliptical (head shaped electrode design(Ra:Rb::3:10) (x, y scale = 10e-4 m)
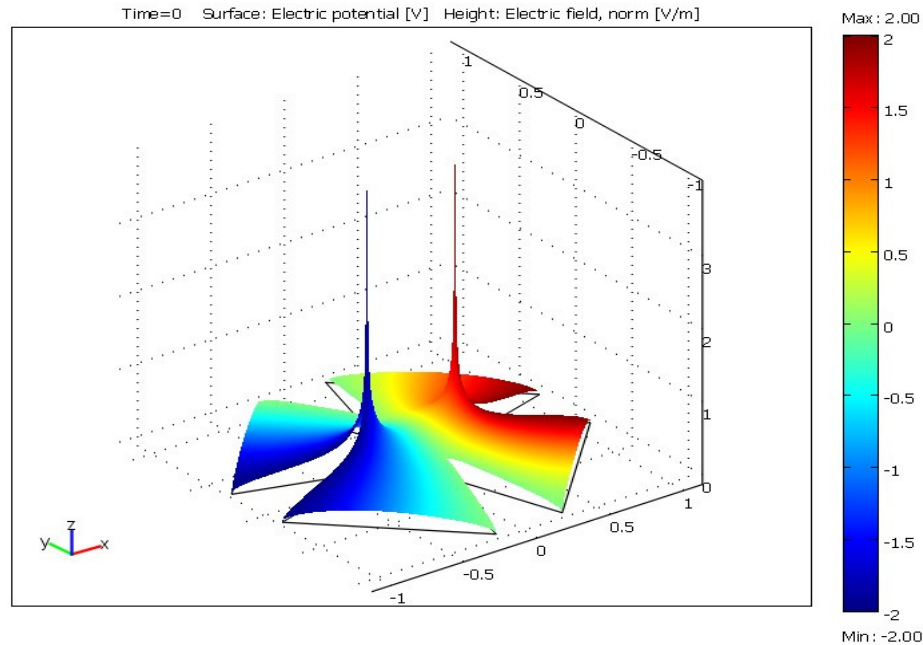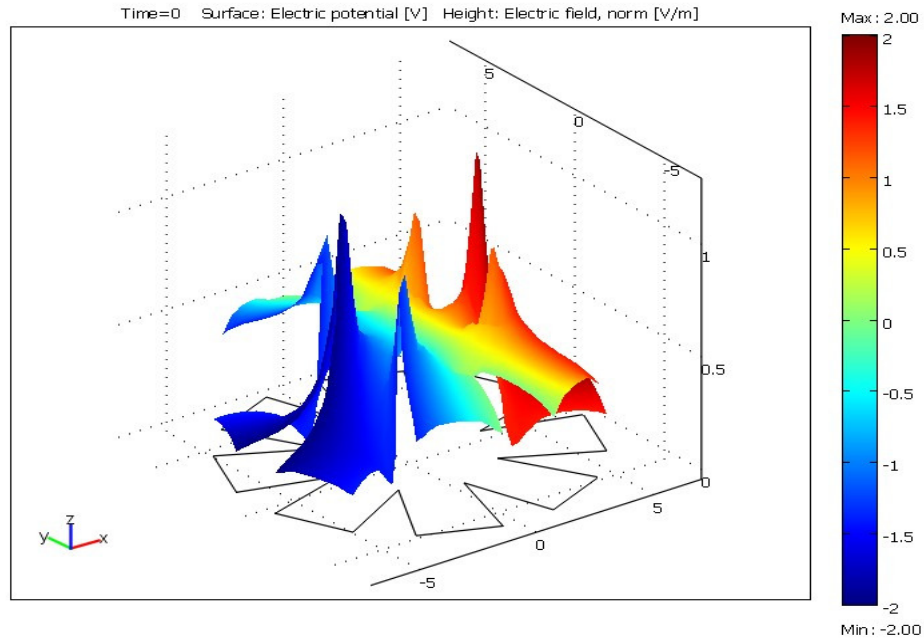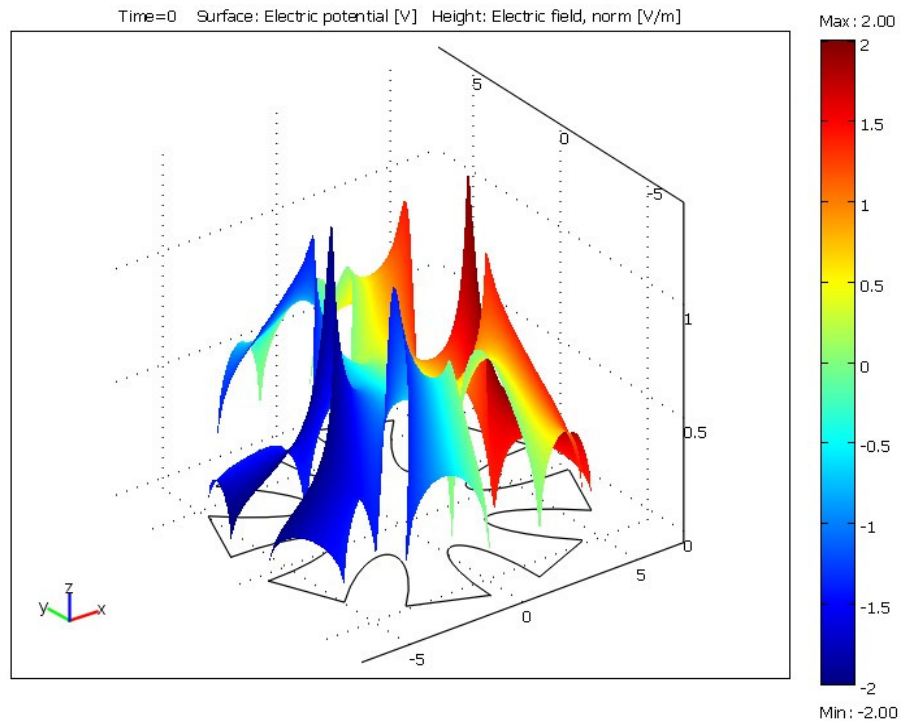

Figure 14. Electric potential and field distribution for 2-D octupole arrow head shaped electrode design (Ra:Rb::3:10) (x, y scale = 10e-4 m)

Figures 13 and 14 show the surface plots of electric potential distribution and 3-D height data determined by the magnitude of the electric field values of the 2-D quadrupole and octupole arrow head electrodes with $R_a:R_b::3:10$ respectively. The height data clearly indicates that octupole electrodes have better trapping than quadrupole electrodes.

2.2.1.3 Flat and concave shape

The flat and concave shaped electrodes were simulated using a set of 2-D designs keeping one radius constant R_a and varying the other radius R_b. The R_a of quadrupole electrodes was 22.5µm and that of octupole electrodes was 10.8µm. The R_a to R_b ratio of the electrode shape was varied from 3:0 to 3:5 and the results obtained were analyzed.
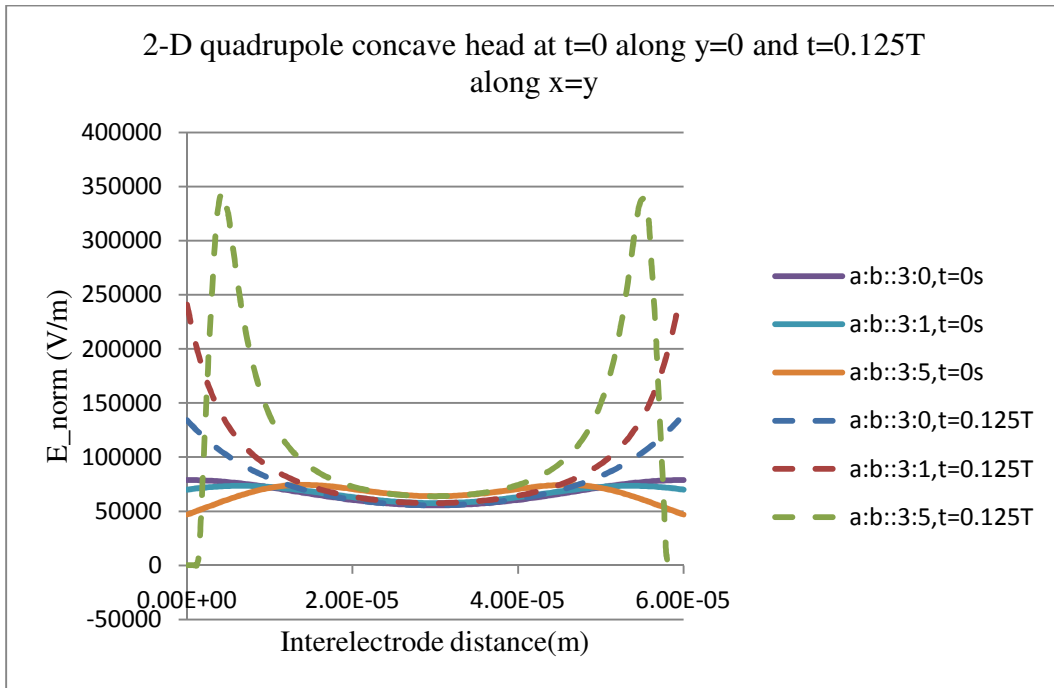
Figure 15. 2-D E_{norm} plot of flat and concave head shaped quadrupole electrodes at t=0s along y=0 and at t=0.125T s along x=y line.

In Figure 15, the E_{norm} distribution is plotted for three geometries at t=0s along the line y=0 and at t=0.125T s along x=y line. The R_a to R_b ratios for the geometries are 3:0, 3:1 and 3:5. Since there is no tip in the concave electrode designs, it is observed that the E_{norm} values drop near the electrode, which will result in poor trapping of the cell due to low DEP force. The octupole flat head electrode design, which has good E_{norm} gradient values, was also fabricated in design iteration 5.
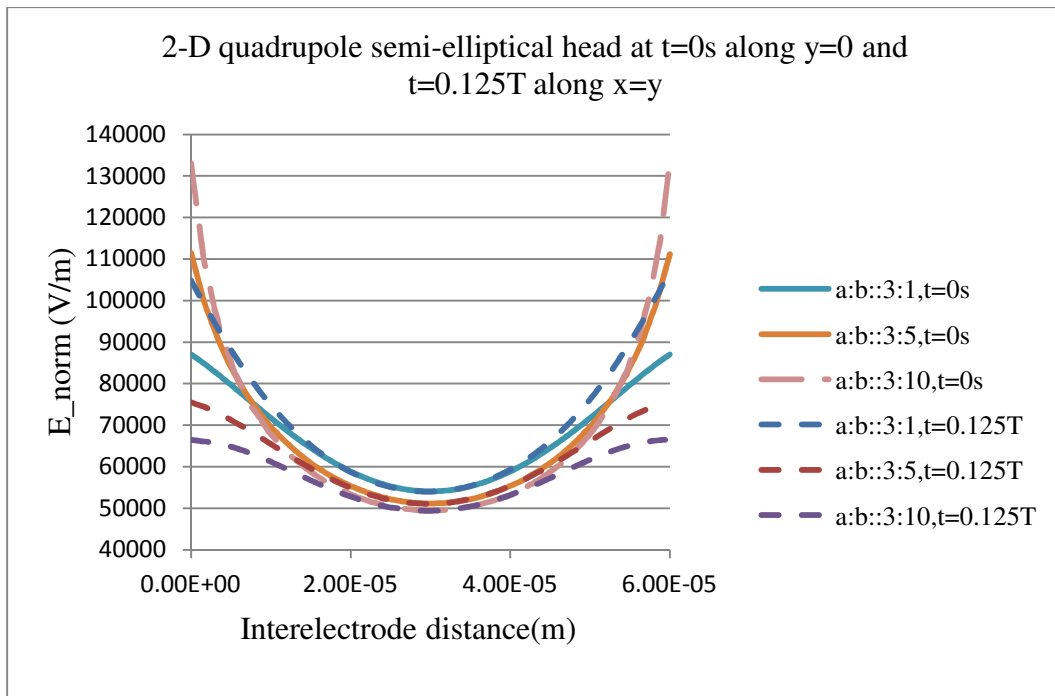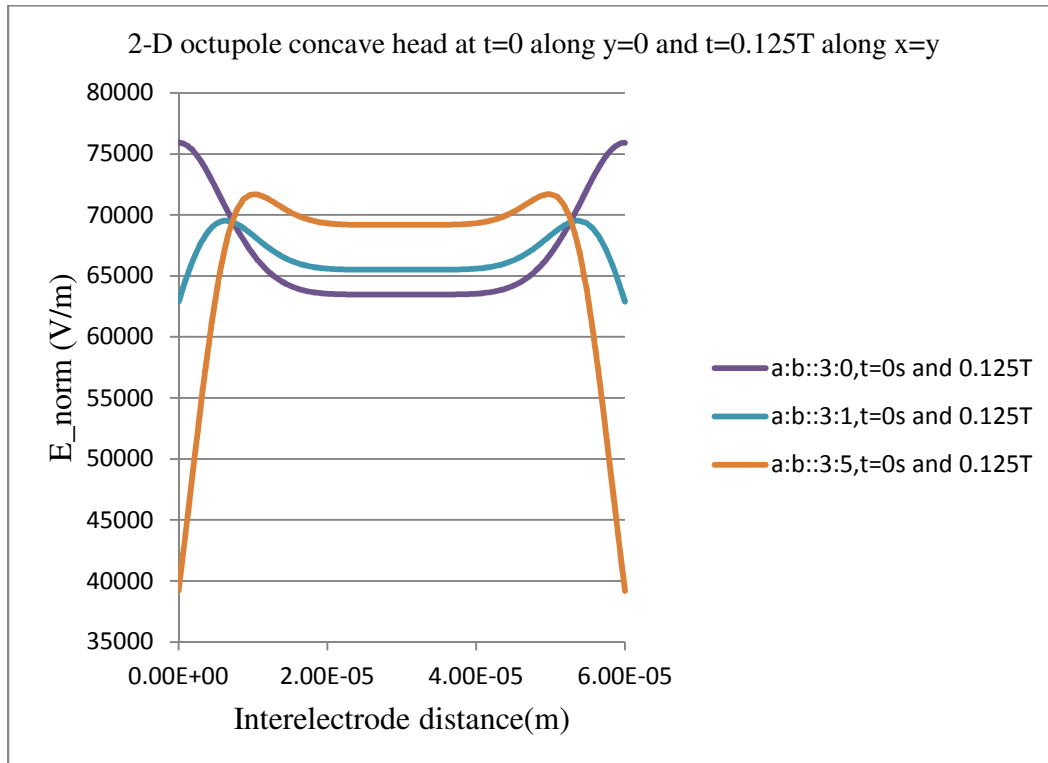

Figure 16. 2-D E_{norm} plot of flat and concave head shaped octupole electrodes at t=0s along y=0 and at t=0.125T s along x=y line.
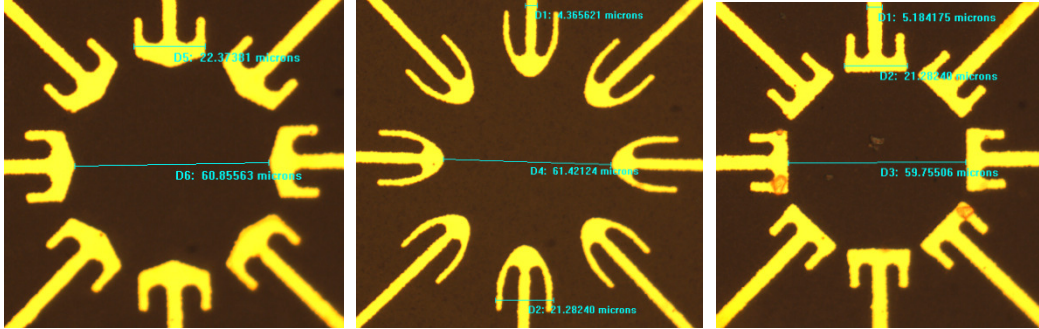
Figure 17. Fabricated arrow, semi-elliptical and flat electrodes of design iteration 5

Using the simulation results, the design iteration 5 was finalized and fabricated to form a 3-D hexadecapole ROT chip. Figure 17 shows the three electrode designs of design iteration 5.

2.2.2 Electrode phase configurations

The electrode phase configuration determines the axis of electrorotation. For imaging purposes, the axis of rotation must be perpendicular to the direction of imaging. While there are a myriad possible electrode phase configurations that can be used to drive the 3-D octode (2 planar quadrupole) or 3-D hexadecapole (2 planar octupole) electrodes, only a countable number of configurations form a closed electrode cage. 3-D electrorotation and/or trapping along different axes in the electrocage are possible. The following guidelines should be considered in order to form a closed electrocage.

1) The trapping forces from all the electrodes along the axis of rotation should be equal.

2) The electric field magnitude at the center of the cage should always be the lowest in the electrocage.

32

Considering the above guidelines, the most stable configuration for rotation along an axis perpendicular to the direction of imaging is given by configuration 1 in Table 2. It is to be noted that due to the symmetry of electrodes, the same configuration can be used for electrorotation along different axes. For stable trapping with no rotation, configuration 2 can be used. Figure 18, shows the 3-D electrode numbering for applying appropriate phase shifts. Figures 19 and 20 show the electric field distribution at the Z=0 plane (central plane) of a 3-D flat head octupole electrocage with interspacing and height as 60µm simulated with configuration 1 and 2 respectively. For the simulation, the Laplace equation as mentioned in the previous section was solved to find the electric field distribution. Using the electrostatics physics, the permittivity of the medium was set as 80.2 (water) and all the other boundaries, except the electrodes, have distributed capacitance with V_{ref} =0 and ε_r as 80.2 for the boundary condition.

Table 2. Octupole electrode configurations

Conf	Elec 1	Elec 2	Elec 3	Elec 4	Elec 5	Elec 6	Elec 7	Elec 8
1	90°	180°	0°	270°	0°	270°	90°	180°
2	0°	180°	0°	180°	180°	0°	180°	0°
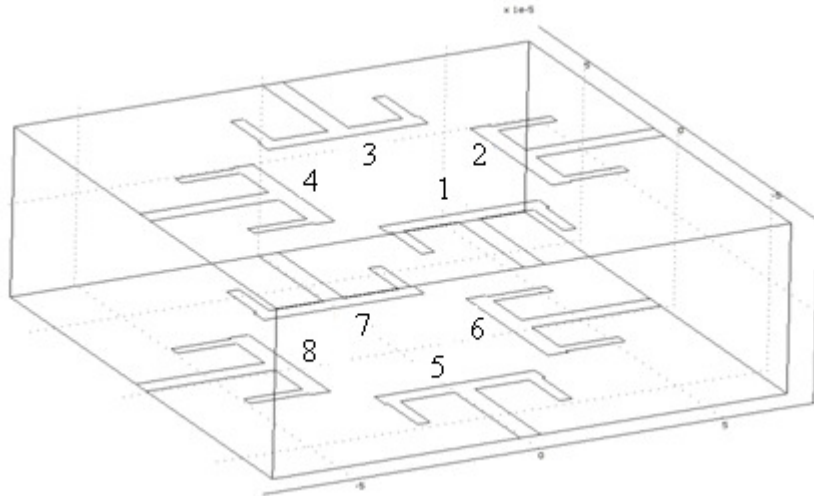
Figure 18. 3-D Electrocage skeleton diagram

33
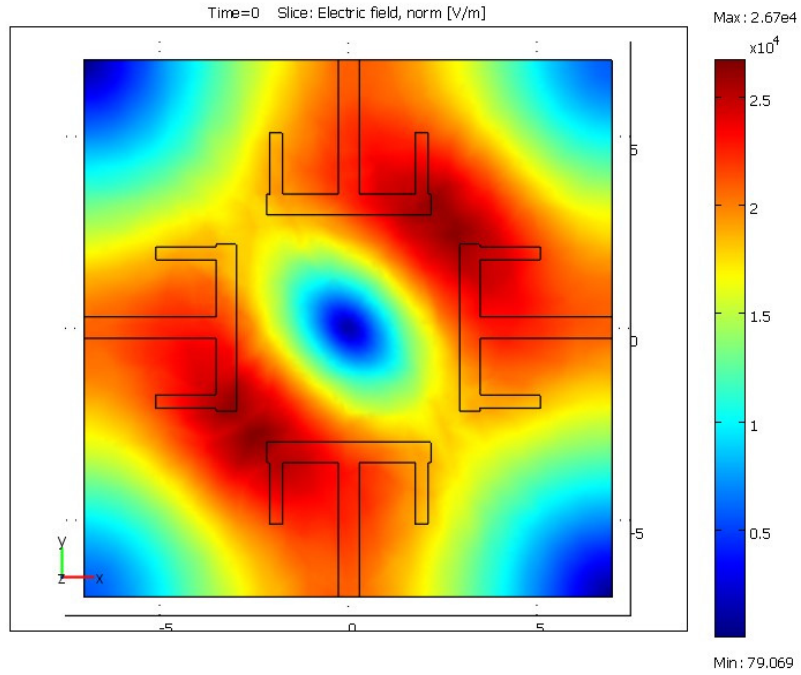
Figure 19. E_{norm} value of 3-D flat head octupole electrocage with phase configuration 1 for electrorotation perpendicular to Z-axis along X=-Y line. (x, y scale = 10e-4 m)
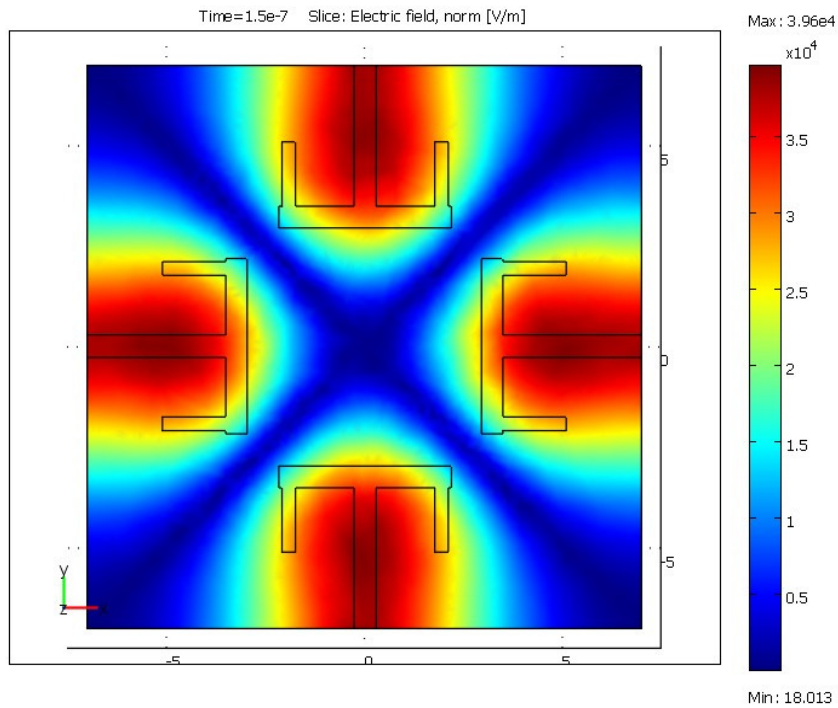
Figure 20. E_{norm} value of 3-D flat head octupole electrocage with phase configuration 2 for stable trapping. (x, y scale = 10e-4 m)

2.2.3 Clausius-Mossotti factor

The Clausius-Mossotti (f_{CM}) factor determines the frequency dependence of the dielectrophoretic force and torque as explained in Section 1.3.1. The dipole approximated f_{CM} for a cell suspended in mediums of different conductivity values has been calculated. The cell was modeled as a sphere with single membrane. As shown in Figure 21, the cell and medium parameters were adopted to be membrane thickness = 8nm, ϵ_{int}=50, σ_{int}=0.5 S/m (Cytoplasm), ϵ_{mem}=8, σ_{mem}=3*10^{-6} S/m (cell membrane) and ϵ_{ext}=78.5, σ_{ext}=1.5*10^{-6} − 1.5 S/m (medium). These values have been used to model the dielectrophoretic response of L929 mouse fibroblast cells (Glasser and Fuhr 1998). The diameter of the cell was considered to be D = 30µm.

The Clausius-Mossotti factor equation mentioned in Section 1.3.1 considers a homogeneous sphere suspended in a medium. Therefore, it is necessary to find the equivalent complex permittivity of a homogeneous sphere that can represent the cell with a single membrane. The equation below shows the expression for equivalent complex permittivity of a cell ($\overline{\epsilon}_c$) (Jones 1995, pg 228).

$$\overline{\epsilon}_c = \overline{\epsilon}_{mem} * \left[\frac{a^3 + 2 * \left(\dfrac{\overline{\epsilon}_{int} - \overline{\epsilon}_{mem}}{\overline{\epsilon}_{int} + 2 * \overline{\epsilon}_{mem}} \right)}{a^3 - \left(\dfrac{\overline{\epsilon}_{int} - \overline{\epsilon}_{mem}}{\overline{\epsilon}_{int} + 2 * \overline{\epsilon}_{mem}} \right)} \right]$$

In the above equation $\overline{\epsilon}$ is the complex permittivity and a = R1/R2. Figure 22 shows the f_{CM} versus log of linear frequency (f) for a cell suspended in medium

of different conductivity. The real (Re[f$_{CM}$] – solid line) and imaginary (Im[f$_{CM}$] – dashed line) part of the f$_{CM}$ has been plotted for medium conductivity values from $1.5*10^{-6}$ – 15 S/m in multiples of 10.
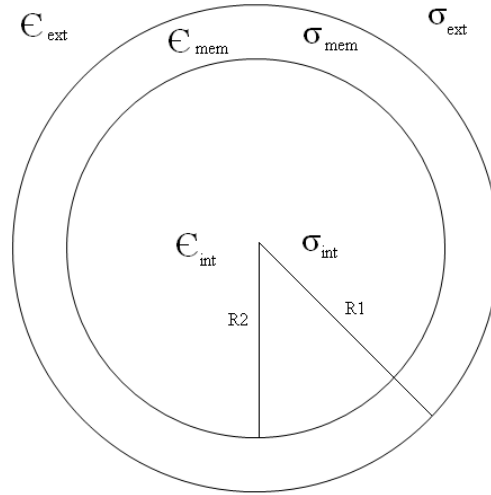
Figure 21. Cell model for Clausius-Mossotti factor calculation

From Figure 22, the complex dependence of the dielectrophoretic forces to frequency are evident. Importantly, the figure shows that the high conductivity of cell mediums aids in slower rotation and maximum trapping with negative DEP which avoids the cell from exposure to high electric fields. And with decrease in the medium conductivity, the cells experience positive DEP and very high rotation torques which can damage the cell. Considering the case where the medium conductivity (σ_{ext}) = 1.5 S/m (approximate conductivity of frequently used cell mediums), the Re[f $_{CM}$] (determines the DEP repelling force that traps the cell) is approximately -0.3 in the frequency range of interest (500kHz - 20MHz) but the Im[f$_{CM}$] (determines the ROT torque that rotates the cell) has a maximum and minimum at 1MHz and 10MHz respectively. Experimental results that have been obtained as described in Section 4.2 using K-562 leukemia and

36

Murine cells have an increasing rotation rate from 500 kHz to 20 MHz as shown in Figures 38 and 39. It is desired to have the slowest rotation possible with maximum trapping for proper imaging. This implies that the frequency of operation should be kept as low as possible ($\leq$ 5MHz) which will be limited by the electrolysis of cell medium (Joule heating) and transmembrane potential of the cell for an applied voltage (Muller et al. 1999).
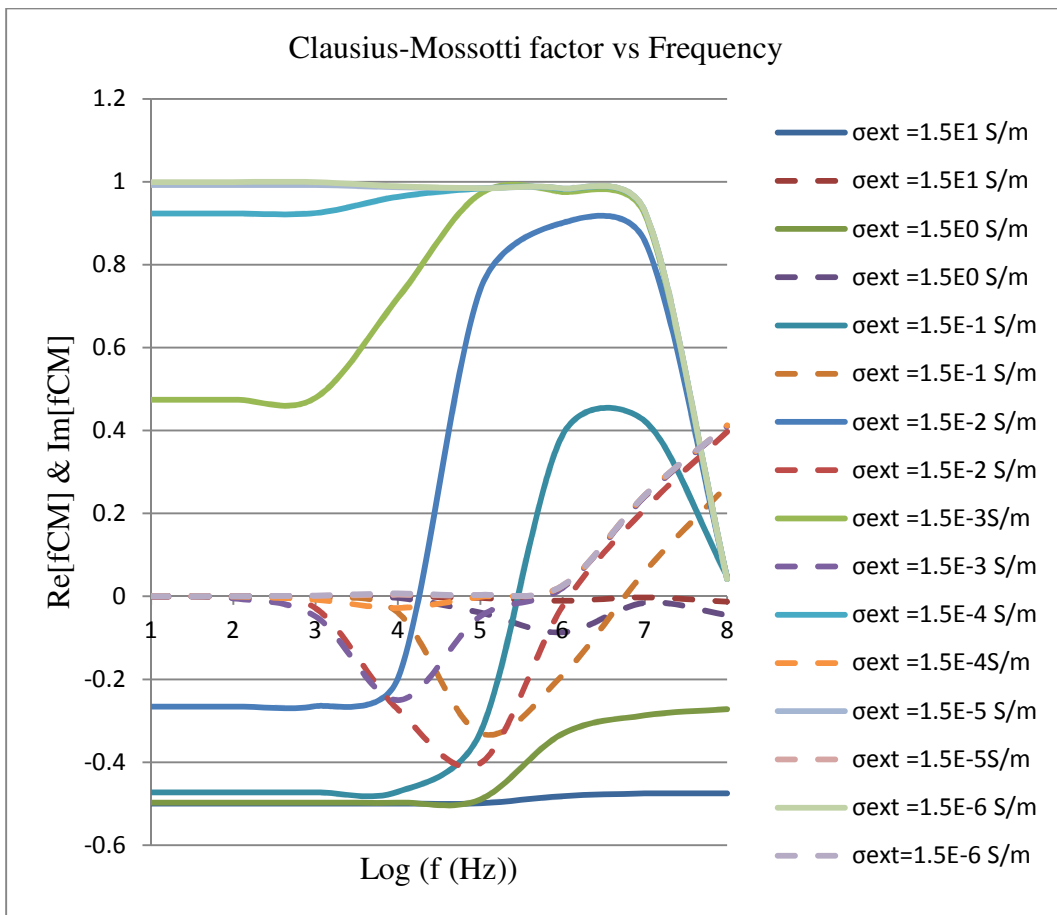
Figure 22. Clausius-Mossotti factor versus log of frequency

2.2.4 Dielectrophoretic force and ROT torque

The DEP force and ROT torque equations have been explained in Section 1.3.1. In this section, time dependent dipole approximated DEP force and ROT torque distribution for a 15µm cell (same permittivity and conductivity values from pervious section) suspended in a medium of conductivity 1.5 S/m has been plotted. The force and torque values were calculated for a 2-D flat head octupole electrode with a rotating electric field configuration (45° phase shift between adjacent electrodes) using COMSOL 3.4. The electric field magnitude ($E_{norm}(t)$) distribution was calculated using the electrostatics application mode with same parameters and conditions used in Section 2.2.1. The distribution was used to calculate the instantaneous force and torque values that will act on a 15 µm cell centered at that particular point.
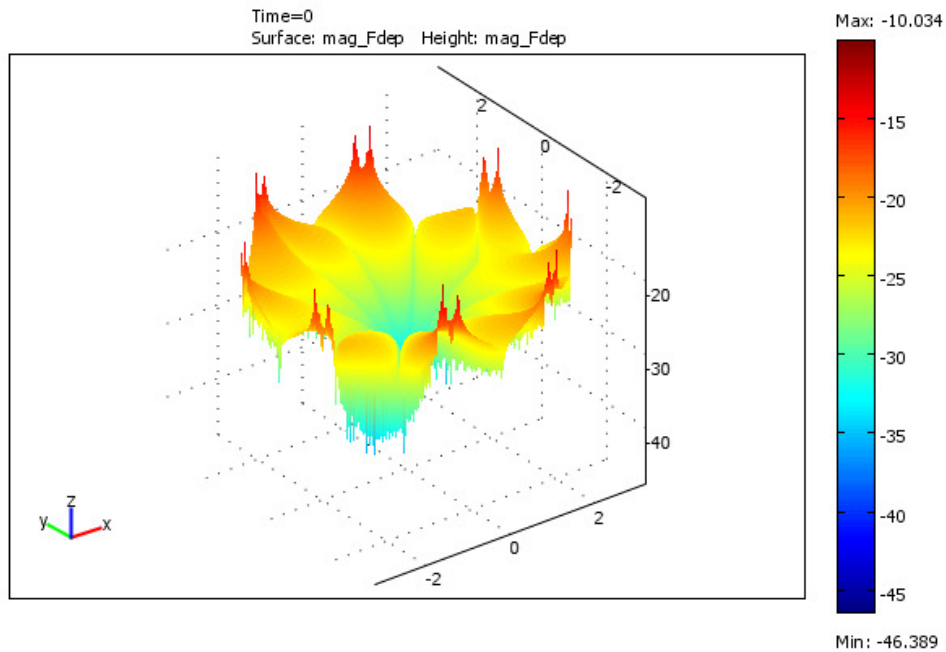
Figure 23. Distribution of log ($|F_{DEP}(t)|$) in 2-D flat head octupole electrode design
(x, y scale = 10e-4 m)

Figure 23 is a 3-D plot of log ($|F_{DEP}(t)|$) force distribution. The outline of the octagonal electrocage is shown for reference. It can be observed that the F_{DEP} force is maximum near the electrodes and minimum at the center of the electrocage. Thus the cell inside the electrocage will be repelled to the center of the electrocage and trapped. The levitation force will not be reflected in this plot as the force is calculated with dipole approximation. Higher order moment contributions to the force have not been calculated here. It is also to be noted that, the planar octupole electrodes have good trapping from all directions enhancing control as compared to planar quadrupole electrodes.
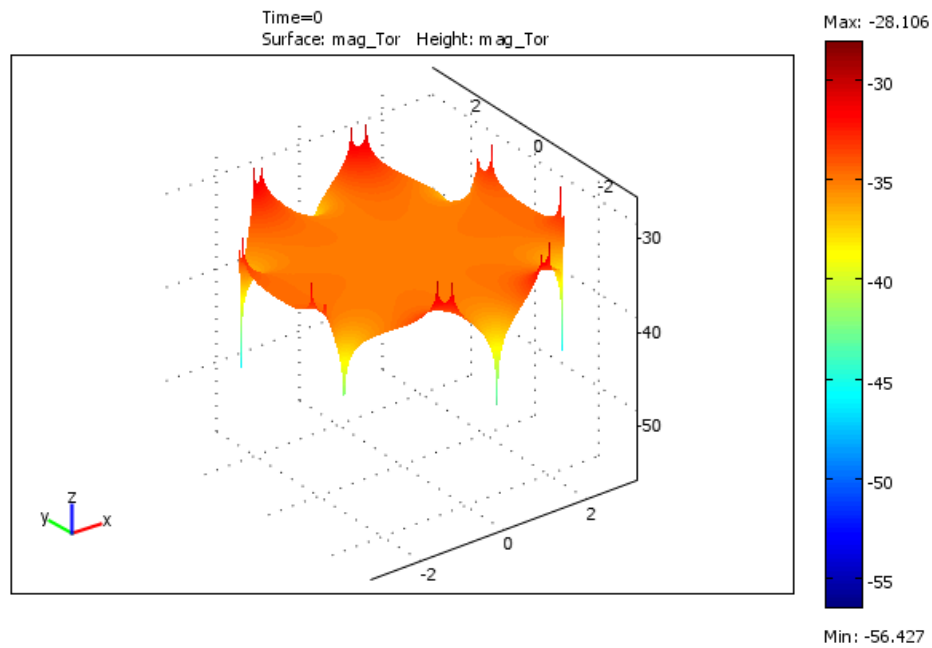
Figure 24. Distribution of log ($|\vec{N}(t)|$) in 2-D flat head octupole electrode design
(x, y scale = 10e-4 m)

Figure 24 shows the 3-D plot of log ($|\vec{N}(t)|$) ROT torque distribution. It can be observed that the torque is maximum near the electrodes tips and nearly

constant in the electrocage area. Thus a cell inside the electrocage will rotate at a steady rate unless it gets very near to the electrodes. Typically, the cell is trapped at the center due to F_{DEP}, but if the cell moves near the electrodes under the influence of external forces like fluid drag or thermal convection, the rotation rate increases rapidly which has also been observed experimentally.

2.2.5 Joule heating simulation

Since Joule heating is caused by the flow of ions in the medium, it was simulated by coupling the Conductive media DC physics (EMDC) and General heat transfer physics (HTGH) in COMSOL 3.4. The voltage and frequency was set to 4V p-p and 20 Hz (due to the expensive computation required for long time spans). A 2-D cross-section of the electrocage was simulated. The EMDC physics assumes that the medium is resistive (with no reactance) and solves for the continuity equation of point form Ohm's law given below to determine the electric field distribution.

$$-\nabla.(\sigma\nabla V - J^e) = Q_j$$

Where, $\nabla.$ is the divergence operator, σ is the electrical conductivity of medium, V is the potential, J^e is the externally generated current and Q_j is a current source.

In the above equation, it was assumed that there is no external current or a current source ($J^e = Q_j = 0$). The resulting equation was solved and the electric field distribution in the electrocage was determined. The electric field distribution obtained is fed as an input to HTGH. The heat source in HTGH is given by the value $\sigma_m * E^2_{norm.}$ In HTGH, the thermal conductivity of the medium

was set to that of water. The medium electrical conductivity (σ_m) was set as 1.5 S/m. The boundary condition for the wall was set as convective flux and for the electrodes as a heat flux. The equation below was solved for in the Joule heating model.

$$\nabla \cdot (-k\nabla T) = Q - \rho C_p u \cdot \nabla T$$

In the above equation, k is the medium thermal conductivity, T is the temperature, Q is the heat source, ρ is medium density, C_p is the medium heat capacity at constant pressure and u is the medium velocity. The velocity field was assumed to be zero and the model was simulated to find the temperature distribution in the electrocage.
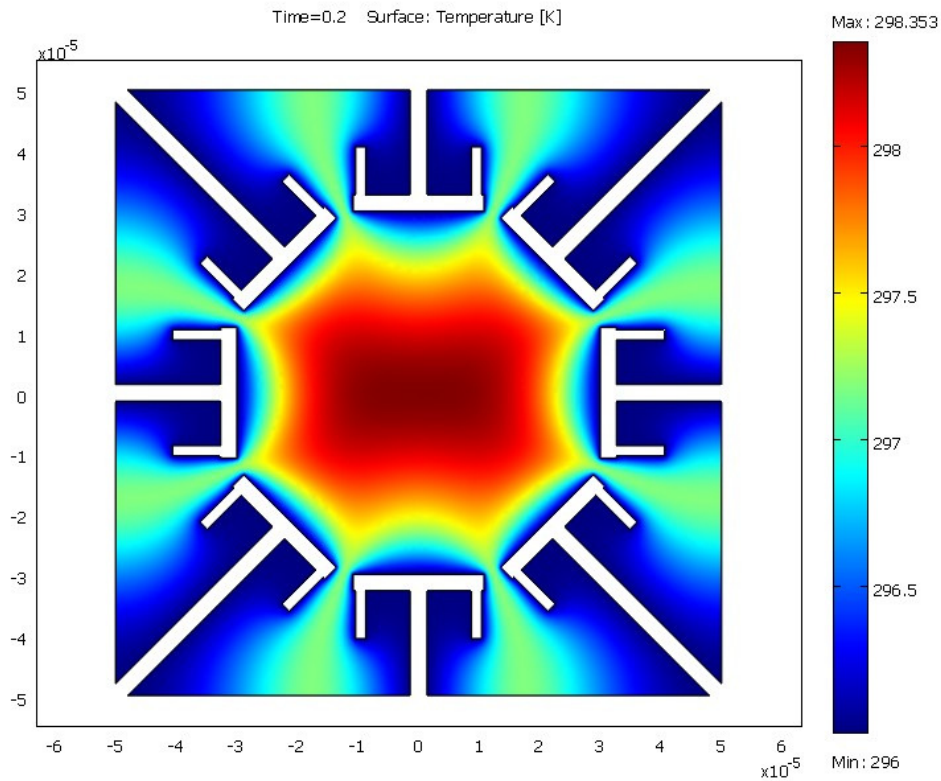
Figure 25. 2-D Temperature distribution in ROT chip due Joule heating.

In Figure 25, the temperature distribution using 2-D Joule heating simulation has been shown. The temperature is at a maximum in the center of the electrocage. This can be attributed to the fact that the center of the electrocage sees the heating effect due to all the electrodes. The electrode regions are cooler as the electric field distribution is lower. Also, the heat generated due to electron flow in the metal is negligible compared to ion flow in the medium owing to the bigger size leading to less mobility. The temperature value is time dependent but reaches a maximum of 2.35 K increase as shown in the figure. But, comparing to the experimental results, the temperature rise predicted by the model is lower. However, the temperature distribution is similar to what is observed experimentally and the temperature is at a maximum at the cage center than elsewhere in the ROT chip.

2.3 Discussion

The F_{DEP} force, ROT torque and Joule heating which are the major electrokinetic phenomena that that determine the electrorotation of cells have been simulated using COMSOL 3.4. The various parameters that affect F_{DEP} and ROT torque including electrode design, Clausius-Mossotti factor and phase configuration has been analyzed leading to logical directions for optimal design and operation of the ROT chip. Very simple models have been used for the simulation. But, the simulation results of the various phenomena follows the same trend as that of the experimental results observed (discussed in chapter 4). Also, the overall design of the ROT chip has been improved through several design iterations for better electrical, fluidic interface and fabrication yield.

42

Chapter 3

Fabrication methods and experimental setup

The fabrication of the ROT chip involved a number of semiconductor technology processes and tools at the Center for Solid State Electronics (CSSER, ASU). The main processes in the manufacture of the ROT chip are electrode and microchannel fabrication, bonding of chip halves, and electrical and fluidic interfacing. It is necessary to develop a robust, repeatable fabrication process for the following reasons.

a) Electrode designs have a critical dimension smaller than 10µm.

b) Control on the height and uniformity of the microchannel is very critical as it determines the symmetry of the electric field distribution and the quality of chip bonding.

c) Precise alignment of the chips is mandatory for forming a good electrocage.

d) Efficient electrical and fluidic interfacing allows for good electrical contact, fluidic containment, and plug-and-play style use of the ROT chip.

3.1 Materials selection

3.1.1 Substrate

Since the ROT chip will be used for optical imaging, which requires high transparency, glass is an ideal substrate (Zahn 2009, pg 19). Since high magnification, low working-distance objectives will be used, the thickness of the

glass must be kept to a minimum for optimal imaging. For testing purposes, standard 4" 500µm thick Borofloat glass wafers are the best choice, due to their better durability.

3.1.2 Electrode metal

Gold was chosen for the electrode material due to its excellent electrical conductivity, chemical inertness, and biocompatibility. However, gold has poor adhesion to glass, requiring an adhesion promoter. A chromium layer has been deposited beneath the gold for this purpose (Zahn 2009, pg 161).

3.1.3 Microchannel

The main constraints in material selection for the microchannel include biocompatibility, high aspect ratio patterning, film uniformity, adhesion to substrate and bond strength. Considering the above constraints, Polydimethylsiloxane (PDMS), SU-8 negative photoresist, KMPR negative photoresist and ACA adhesive film were considered for the microchannel fabrication. In spite of excellent film uniformity with PDMS (plasma treated) and ACA adhesive film, the adhesion to glass is instantaneous which makes it difficult to perform alignment before bonding. Therefore, SU-8 and KMPR epoxy based, high aspect ratio, negative tone photoresists were considered for the microchannel fabrication. These photoresists have been extensively used in biomicrofluidics (Abgrall et al. 2007; Zahn 2009, pg 20-22; Juang, Huang, and Chen 2010).

3.2 Process characterization

3.2.1 Gold deposition process

Chromium (adhesion layer) and gold were deposited using thermal and e-beam evaporation techniques. Edwards-2 thermal evaporator and CHA e-beam evaporator at CSSER were used to deposit and analyze the quality of the gold film. It was observed that the durability and pinhole defect density varied considerably between the gold films obtained using the tools. All the depositions using the two tools were done under the recommended deposition pressure of 3e-6 Torr at a rate of 0.1nm/s or lesser to obtain a very conformal layer with minimum pin-hole defects. And the thickness of chromium and gold deposited was 20nm and 200nm respectively. A comparison of the two evaporator tools for gold deposition is shown in Table 3 below.

Table 3. Edwards-2 thermal evaporator versus CHA e-beam evaporator

Edwards-2 thermal evaporator	CHA e-beam evaporator
Only one 4-inch wafer can be deposited at a time significantly increasing the process time.	18 4-inch wafers can be loaded and deposited with gold simultaneously significantly reducing process time.
Approximately 1 gram of gold is required to deposit one 4-inch wafer.	Approximately 8g of gold is required for deposition of the 18 4-inch wafers.
Slight non-uniformity in gold film across wafer may result due to stationary parts during deposition.	Samples loaded on rotating carousal during deposition which improves the uniformity of the gold thickness.
Minimal Pin holes when deposition rate is $\leq$ 0.1nm/s as shown in Figure 26 a.	High pin hole density even when the deposition rate is $\leq$ 0.1nm/s as shown in Figure 26 b.
Good film durability and requires no annealing.	Relatively poor film durability and requires 1 hr annealing at 250 °C in a furnace as shown in Figure 27.
Molybdenum boat holder (gold source) avoids particulate contamination during deposition.	Graphite crucible holder (gold source) is a source of carbon particulates adulterating the gold and deposition process.
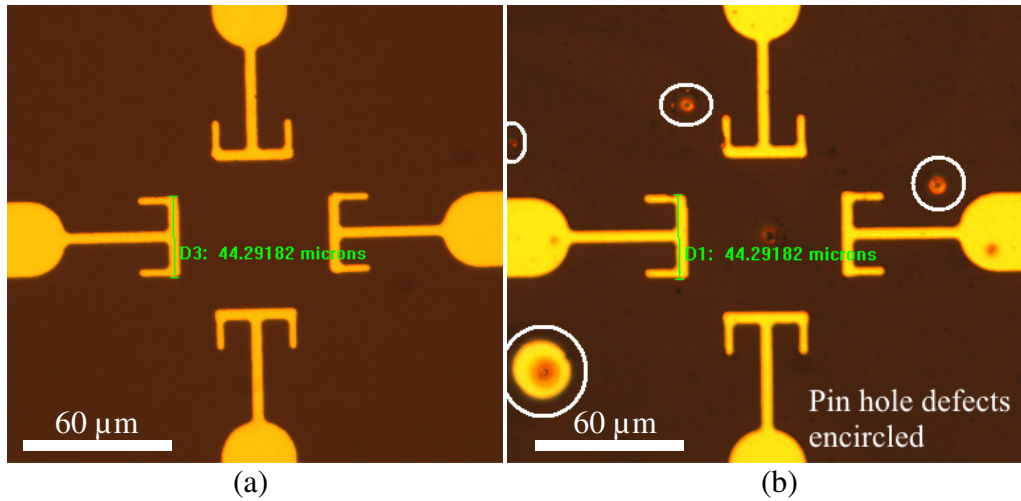
Figure 26. Pin-hole defect density- Edwards-2 (a) versus CHA evaporator (b).
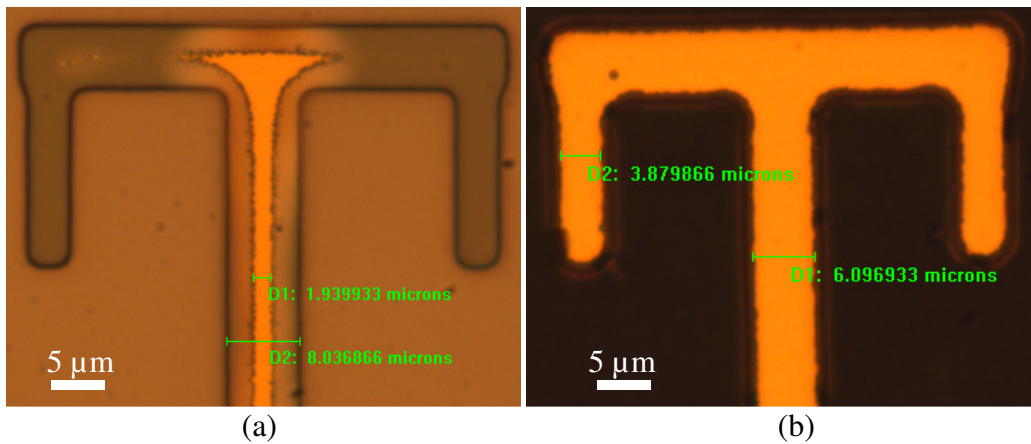
Figure 27. Effect of annealing on CHA evaporator deposited gold film, (a) without annealing, (b) with annealing.

As shown in Figure 26, Edwards-2 yields a durable and defect free gold film as compared to CHA evaporator which yields a gold film with many pin-hole defects and requires an additional annealing process to improve durability as shown in Figure 27. On the other hand, the lower process time, lower cost and high throughput are the advantages offered by the CHA e-beam evaporator tool.

3.2.2. Gold etching process

The gold and chrome etching were done using wet etching methods due to their low-cost and high etch rates. For gold etching, aqua regia (1:2:3 -- HNO_3: H_2O: HCl) and commercially available TFA gold etchant (Transcene company, Inc.) were used. Aqua regia had relatively unpredictable etch rates with large undercutting as shown in Figure 28 a. The TFA gold etchant had a constant etch rate of approximately 2.8 nm/s with minimal undercutting as shown in Figure 28b. To compare the etchants, gold etching was performed on a gold film deposited using Edwards-2 thermal evaporator. For chrome etching, commercially available chrome etchant (Cyantec, Inc.) was used which offered constant etch rate and minimal or no undercutting.
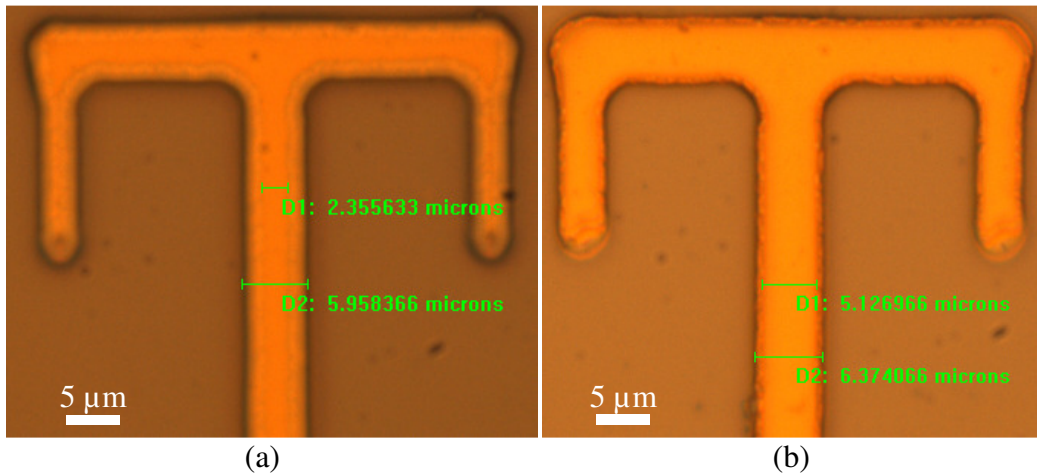
Figure 28. Gold wet etching – Aqua regia (a) versus TFA gold etchant (b).

3.2.3 Microchannel fabrication

Even though SU-8 and KMPR photoresists are used extensively in biomicrofluidic applications, a comparison of the two photoresists (in Table 4)

was required to determine which was optimal for the fabrication of the ROT chip (Chollet 2009; Ray, Zhu, and Elango 2011).

Table 4. SU-8 2035 versus KMPR 1025 for ROT chip fabrication

SU-8 2035 photoresist	KMPR 1025 photoresist
Poor adhesion to glass even with an adhesion promoter (AP 3000, HMDS, Omnicoat) result in partial peeling of features.	Good adhesion to glass with hexamethyldisilizane (HMDS) as an adhesion promoter.
Requires slow ramp rates during soft bake and post exposure bake processes to minimize thermally induced stress which causes cracking.	Requires no ramping for soft bake and post exposure bake and minimal thermally induced stress is observed.
More reflow at high baking temperatures (>65 °C) decrease the layer uniformity.	Minimal reflow ensuring good film uniformity even at 100 °C (standard soft bake temperature).
Removing cross-linked SU-8 is tedious. It can be removed only using piranha solution (1:1:: H_2SO_4:H_2O_2).	Cross-linked KMPR can be easily removed using solvent based stripper enabling process repetition upon photoresist failure.

Several different thicknesses of SU-8 and KMPR microchannels have been fabricated, ranging from 40 to 120µm to match electrode interspacing using different photolithography recipes. Nonetheless, the final microchannel thickness was fixed at 60 µm so that the cell was trapped 30 µm from the bottom substrate, enabling the use of low working-distance objectives. From the comparison shown in Table 4, KMPR 1025 offers several advantages and was primarily used to fabricate the microchannel. The recipes shown in Table 5 have been used with SU-8 and KMPR photoresists to obtain a 60 µm microchannel.

Table 5. SU-8 and KMPR recipe for 60 µm height microchannel

SU-8 2035 photoresist 60 µm recipe	KMPR 1025 photoresist 60 µm recipe
Dehydration bake for 15 minutes at 150 ° C.	Dehydration bake for 15 minutes at 150 ° C.
Rest the wafer for 3 minutes.	Rest the wafer for 3 minutes
Apply AP 3000 adhesion promoter and spin coat at 1150 rpm for 40s.	Apply HMDS adhesion promoter and spin coat at 1000 rpm for 60s.

Apply SU-8 2035 and spin coat at 1150 rpm for 40s.	Apply KMPR 1025 and spin coat at 1000 rpm for 60s.
Rest the wafer for 3 minutes.	Rest the wafer for 3 minutes.
Soft bake- ramp from room temperature to 65 °C at the rate of 5 °C/min and continue to bake for 45 minutes at 65 ° C.	Soft bake at100 °C for 15minutes. Rest the wafer for 3 minutes. Bake the wafer again at 100 °C 3 times for three minutes each with 3 minutes gap between each bake.
Expose the wafer to 300mJ/cm^2 exposure dose with PL360-LP filter (Omega Optical).	Expose the wafer 1500mJ/cm^2 exposure dose with PL360-LP filter (Omega Optical).
Post exposure bake- start from 65 °C and ramp to 95° C at the rate of 5° C/min and continue to bake for 6 minutes at 95° C.	Post exposure bake at 95° C for 3minutes and 30 seconds.
Develop using SU-8 developer for approximately 6 minutes.	Develop using MF-26A developer for approximately 6 minutes.
Hard bake at 120° C for 15 minutes.	Hard bake at 120° C for 15 minutes.

3.2.4. Chip bonding

Adhesive bonding techniques are prevalently used to fabricate closed channels from photoresist (Niklaus et al. 2006). In fabricating the ROT chip, two such methods have been explored. The first method made use of an EVG 520 bonder tool to apply heat and pressure causing reflow of the photoresist layer and adhesion between the two chip halves. The second in-house developed method made use of SU-8 2005 photoresist, which was drawn in between the chip halves by capillary action and crosslinked to adhere the chips together. Table 7 compares the two bonding methods tabulating the advantages of each.

3.2.4.1 EVG 520 bonding

The EVG 520 bonder was used for bonding on the wafer (4 inch) scale. The wafers used for testing had 60µm height KMPR/SU-8 microchannels fabricated using the recipe mentioned in Table 5, skipping the hard bake step to maintain some compliance. The wafers were then rinsed with deionized (DI) water in a

dump rinser for 15 minutes before bonding. Plasma cleaning of the photoresist layer using Tegal Ashers tool for 1 minute at 200W and 50sccm oxygen resulted in poor bonding. It was found that plasma cleaning removes remnant uncrosslinked photoresist (after developing) from the surface of photoresist layer (Serra et al. 2007). The uncrosslinked photoresist aids the bonding by increasing the bond strength. For this reason, plasma cleaning of the photoresist layer was removed from the bonding protocol. The DI water rinsed wafers were then positioned and aligned on the clamp unit of the EVG 520 bonder. The aligned wafers were held together using the clamp unit, which was then placed into the bonder and locked. The bonding pressure and temperature applied was varied to achieve optimum bonding conditions. The bonding time and temperature ramp rate was fixed at 60 minutes and 10°C/min respectively. The table below shows the bonding parameters used for the experiments.

Table 6. SU-8 and KMPR adhesive bonding results using EVG 520 bonder

Photoresist	Parameter	Pressure (N)	Temperature (°C)	Results
SU-8 2035	Hard baked	2000	180	No bonding
SU-8 2035	No hard bake, plasma treated	2000	180	No bonding
SU-8 2035	No hard bake, no plasma treatment	2000	180	Good bonding, Figure 29 b
KMPR	No hard bake, no plasma treatment	2000	180	Poor bonding
KMPR	No hard bake, no plasma treatment	1000	120	Good bonding, Figure 29 a
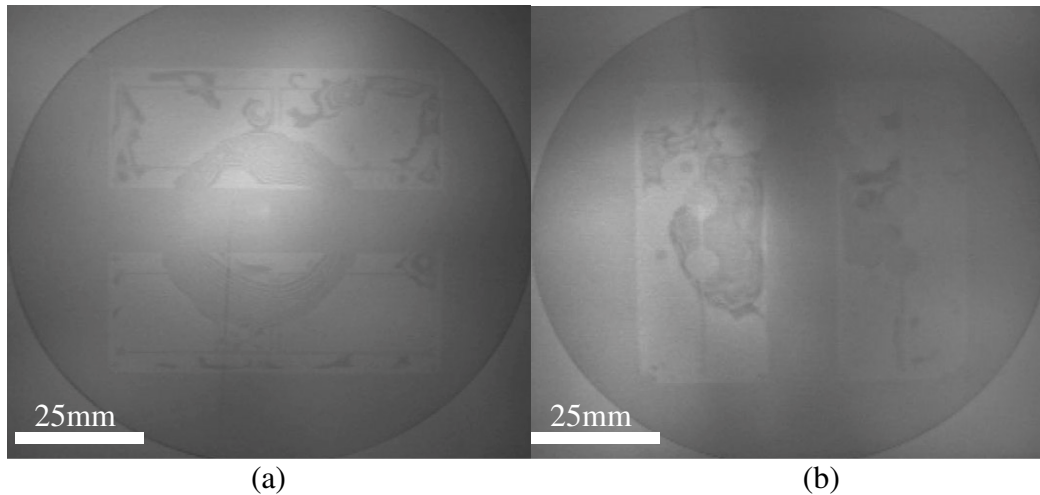
Figure 29. EVG bonding of KMPR(a) and SU-8(b) patterned 4-inch wafers

3.2.4.2 Diffusive bonding

The diffusive bonding technique is based on the capillary diffusion of the SU-8 2005 (low viscosity – 45 cSt) photoresist between two sandwiched chips. The diffusive bonding technique has not been optimized for wafer level bonding. As such, the bonding is done on a smaller scale with chips that have been diced from the 4-inch wafers with a dicing saw. The complementary chip halves that form the 3-D electrocage were aligned using the OAI 200 aligner. The aligned chips were then held in hard contact on the aligner and a few drops of a viscous two part epoxy were applied to the edges of the chips. Once the epoxy cured (cure time = 15minutes), it held the chips aligned. SU-8 2005 was then pipetted along the edges of the chip in small volumes (~5µl). The SU-8 2005 seeped into the chip due to capillary action and spread to the entire chip excluding the microchannel. Then the chip sandwich was soft baked at 40°C for 2 hours to evaporate the solvent (low bake temperature allows the solvent vapors to escape without driving liquid phase SU-8 into the microchannel) and exposed to 100

mJ/cm^2 exposure dose. The sandwich was then post exposure baked for 1 hour at 60°C to achieve a bonded ROT chip. Now the cross-linked SU-8 2005 functions as an adhesive layer to hold the ROT chip together. The cured epoxy was cut away with a rotary tool to free up space for additional processing.
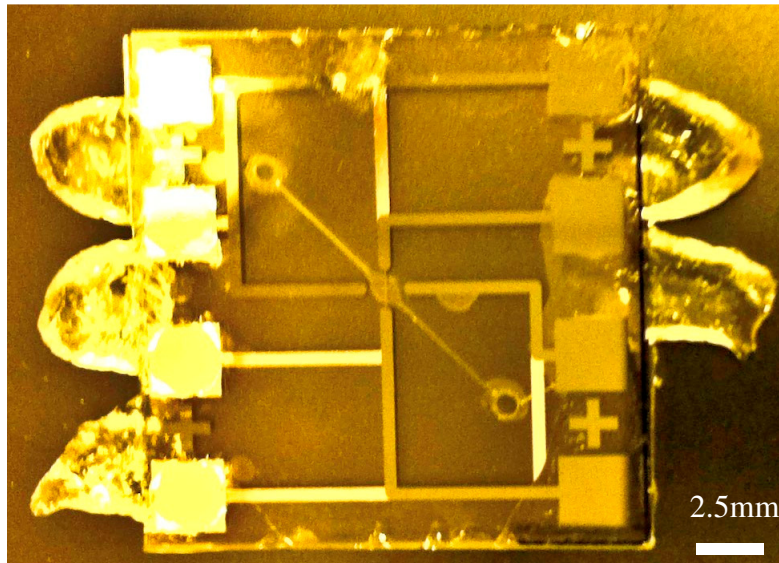
Figure 30. Diffusive bonded ROT chip with two parts epoxy

Table 7. EVG 520 bonding versus Diffusive bonding

EVG 520 bonding	Diffusive bonding
High pressure (~2kN) and relatively high temperature process (120-180 °C).	No applied pressure and low temperature process (60°C).
Requires precise alignment using aligner followed by transfer using clamp unit to bonder before bonding.	Requires precise alignment using aligner and epoxy to secure the aligned chips before bonding.
Due to the large forces involved, misalignment can occur resulting in accuracy of ~ 10µm (Niklaus et al. 2003)	Bonding accuracy is limited by the aligner and the user normally within ~ 2 µm.
Lesser bonded area due to air trapped between the bonded areas and photoresist layer non-uniformity.	Minimal or no air trapped with careful operation and compliance possible for photoresist layer non-uniformity.
Excellent bond strength	Excellent bond strength
High cost process.	Low cost process.
Only wafer to wafer bonding is possible using the bonder tool.	Chip to chip bonding has been optimized. Wafer level bonding has not been optimized.
Channel deformation may occur due to excess pressure with elevated temperatures.	Channel clogging is possible which depends upon the geometry of the microchannel.

The EVG bonding conditions for KMPR photoresist was optimized to be 120 °C and 1kN piston pressure and 180 °C and 2kN for SU-8. Figure 29 shows the EVG bonded wafers with 60 µm KMPR photoresist layer and SU-8 photoresist layer respectively imaged using a transmission infrared camera. The bonded wafers had two rectangular photoresist patterns on them. On these rectangular regions, the light gray region corresponds to bonded area where as the medium and dark gray areas correspond to unbonded areas. The darkness of the area increases with increasing separation of the glass. It can be observed that in both cases only ~ 75% of the area is bonded. This is a result of the non-uniform thickness of the photoresist layer (± 3µm) and air trapped during bonding.

Figure 30 shows the ROT chip with the two-part epoxy holding the sides of a chip that have been bonded using the diffusive bonding technique. It can be observed that there are no air gaps in the bonded area, unlike EVG bonding.

3.2.5 Electric and fluidic interface

Electric and fluidic interfacing is a critical feature of the ROT chip. The electrical and fluidic connections were made possible by laser milling the chips. Using a custom built CNC laser micro-machining tool (MB 1000, Xcaliber)—operating at 355nm and 2W—arbitrary patterns can be cut in various materials through ablative removal of material. For the ROT chip, 1mm diameter holes were cut through the 500µm glass to allow fluidic interfacing with the microchannel. In a similar fashion, larger 3mm diameter holes were cut strategically in both top and bottom halves of the ROT chip to allow access to the

electrode contact region on the opposite chip. Wires were soldered to the electrode contact region through the 3mm holes. Nanoport connectors (Upchurch Scientific, Oak Harbor, WA) were adhered to the fluidic ports using a strong two-part epoxy. The Nanoport connectors allow for the connection of tubing to the ROT chip. This connection is leak free, strong, and reliable, allowing for easy introduction of cells into the ROT chip.

3.3 Fabrication process

Fabrication of the ROT chip requires bonding of two wafers and therefore every batch required two 4-inch Borofloat wafers. The process starts with RCA cleaning of the wafer substrates, done by treating the wafers with a solution of DI water, ammonium hydroxide, and hydrogen peroxide (in the ratio 5:1:1 respectively) at 75°C for 10 minutes to remove organic contaminants and then with a solution of DI water, hydrochloric acid and hydrogen peroxide (in the ratio 6:1:1 respectively) at 75°C for 10 minutes to remove metallic contaminants. The wafers were rinsed in a dump rinser for 10 minutes and dried with nitrogen. This was followed by a dehydration bake at 120°C for 15 minutes. Using thermal or e-beam evaporation tools, chromium was deposited on the wafers (to 20nm thickness) followed by gold (to 200nm thickness), as explained in Section 3.2.1. In the next step, AZ 3312 positive photoresist (AZ electronic materials USA Corp., Branchburg, NJ) was spun on the wafers at 3500 rpm for 30s to 1µm thickness using the P-6708 precision spin coater (Specialty coating systems, Indianapolis, IN). The wafers were then soft baked at 100°C for 1minute on a hot plate. Each of the wafers was then exposed at 45mJ/cm^2 exposure dose using the

EVG 620 photolithography tool (EV Group, Tempe, AZ) with an electrode design photomask to expose and pattern the photoresist layer. The patterned photoresist layer was developed using the AZ 300MIF developer to form the electrode patterns. The wafers were hard baked at 110°C for 1 minute to remove any remnant solvent. The photoresist forms a mask for the gold wet-etching process by protecting the covered areas. Each of the wafers was then etched separately using fresh TFA gold etchant (Transcene, Inc., Danvers, MA) for 70-80 seconds until the exposed gold layer was entirely removed. The etched wafer was then inspected in a microscope for quality. With the gold etched away, the chromium layer beneath remained. The chromium was wet-etched for 20-30s using chrome etchant until the wafer was completely transparent in the exposed areas. In the next step, the wafers were cleaned in Microstrip 2001(Fujifilm, Allendale, NJ) for 5 minutes at 65°C to remove the AZ 3312 layer. The gold electrodes are now clean and fully developed. A 60µm height KMPR 1025 (Kayaku Microchem, Newton, MA) microchannel was then fabricated on the appropriate wafer using the recipe given in Table 5. Because the fabricated KMPR channel is full height and adheres well to glass, it is only fabricated on one of the two wafers. In Figure 31, the complete fabrication process flow is shown.

1) Uncleaned wafers 1 & 2

2) RCA cleaned wafers

3) 20nm Chromium + 200nm Gold deposited wafers

4) AZ 3312 +ve photoresist mask - 1um

5) AZ 3312 photoresist UV exposed and patterned

6) Gold etched in TFA etch + Chrome etched in Cyantec etch

7) Microstripper clean

8) Wafer 1 laser milled for ports

9) Using process steps till 7, wafer 2 spun coat with KMPR -ve photoresist - 50um

10) KMPR -ve photoresist UV exposed and patterned in wafer 2

11) Wafers 1 and 2 bonded using SU 8 -ve photoresist diffuse bonding technique

Note: Features not to scale

Figure 31. ROT chip fabrication process flow

The next step in fabricating the ROT chip was to cut the glass wafer to make fluidic and electric interfacing ports. This was achieved by the procedure explained in Section 3.2.5. Once the holes were cut, the wafers were diced using a dicing saw (Assembly technologies Inc., Orr Road Charlotte, NC) to attain individual chips. Each chip was aligned and bonded with its counterpart using the OAI 200 and the diffusive bonding technique was implemented to form the ROT chip as explained in the Section 3.2.4.2. Wires were then soldered to the electrode pads, and Nanoports were adhered to complete the ROT chip. In Figure 32, the ROT chip (design iteration 1.0) from a wafer to electrocage level is shown.
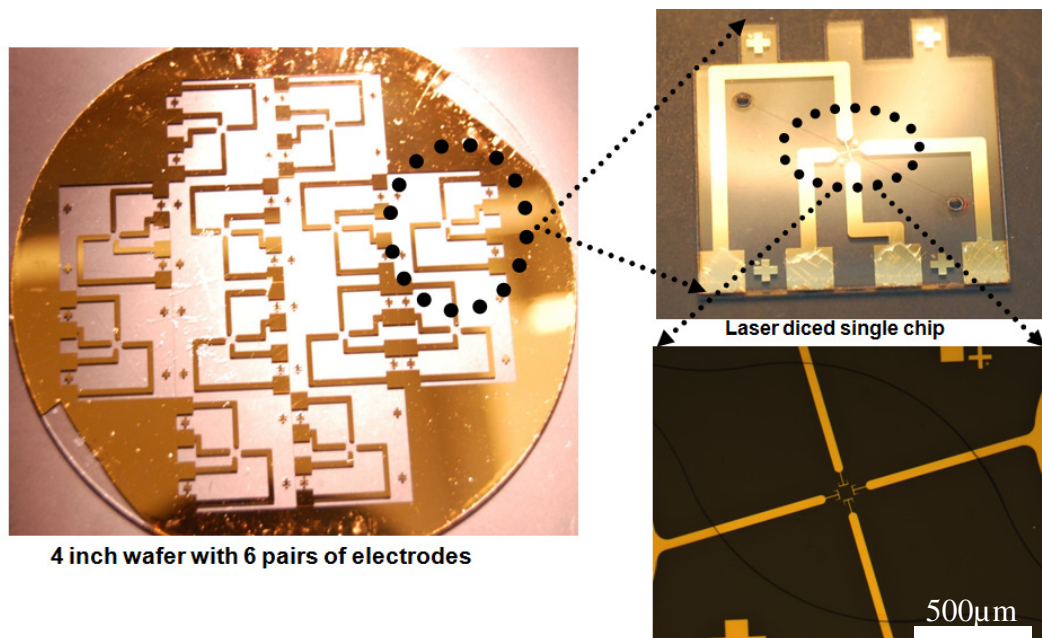
Figure 32. Zoom-in picture of ROT chip from 4" wafer to electrocage

3.4 Experimental setup

The experimental set up consists of the microscope, function generator, camera and PC. All the experiments were conducted on a Nikon TS 100 microscope. The two function generators used were T-340 (Highland technology, San Francisco, CA) (4 output channel, maximum frequency - 2MHz) and PXI 1045 (National Instruments, Austin, TX) (8 output channel, maximum frequency - 20MHz). Both function generators were used to create sinusoidal waveforms. For the T-340, an interactive program was created using LabVIEW incorporating a .NET driver developed in-house to access the functionalities of the generator. With the program, it was possible to set the peak-to-peak voltage, frequency and phase shift of the four channels separately and in real-time. With PXI 1045, another program was written using LabVIEW which made use of the FGEN driver provided by National Instruments to synchronize and control the eight

individual generator modules. The LabVIEW program enabled the user to change the peak-to-peak voltage, frequency and phase of all the eight channels, after which the synchronization is performed. Once the synchronization process is finished, desired voltages were available at the outputs of each generator. Video acquisition was carried out with the Prosilica GE 1650 camera (AIA, Ann Arbor, Michigan) driven using Prostream software (Southern Vision Systems, Inc., Snellville, GA). The NI PXI has an in-built PC which was used to drive all the generators (including T-340) and the camera. In Figure 33, all the constituents of the experimental set up are shown. Figure 34 shows a ROT chip, with syringes attached to the Nanoports, loaded on the TS 100 for testing. Cells are flowed into the chip using the syringes and the BNC grabbers from the function generator are used to power the electrodes.
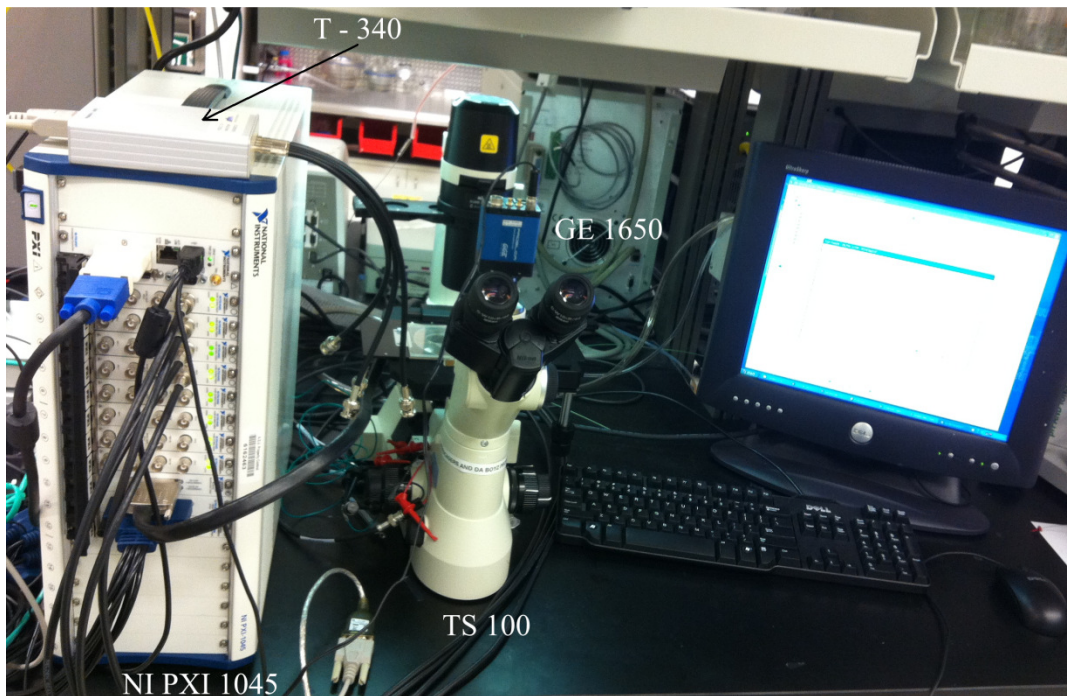
Figure 33. Electrocage experimental set up
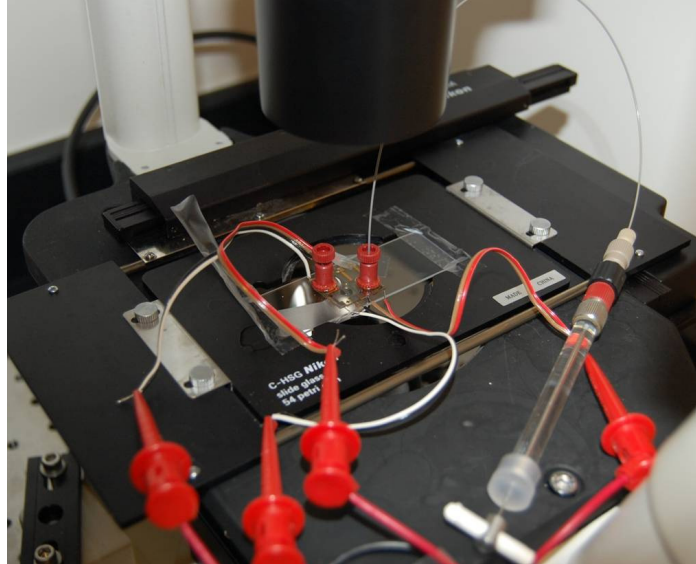
Figure 34. TS 100 test bed showing ROT chip with electrical and fluidic
connections.

3.5 Discussion

Various materials and process steps involved in the fabrication protocol
have been analyzed in detail and optimized for manufacture of a fully functional
ROT chip with good repeatability. However, with the current fabrication method
and experimental setup the low throughput (9 ROT devices for a batch), long
process times (approximately 20 hours from blank wafer to working ROT device),
cell delivery and cell retrieval have to be improved. Reducing the form factor of
the chip and enabling wafer level bonding can considerably improve the through
put and process time. Also, with the current ROT chip manufactured, using high
magnification objectives is not possible due to the use of 500µm thickness wafers
and has to be transferred to 170µm thickness substrates.

Chapter 4

Cell rotation characterization

The aim of the experiments conducted using the ROT chip was to characterize cell rotation in the presence of applied AC electric fields and determine the rotation rate dependence on relevant electrical parameters. Considering the DEP force and ROT equations, the variables that affect the rotation rate include applied voltage and frequency, cell size and shape, permittivity of cell and medium, conductivity of cell and medium, electrode shape and spacing, number of electrodes and phase configuration.

To allow for imaging, a cell rotation rate on the order of 1/60Hz is required, as well as a fixed axis of rotation perpendicular to the imaging axis with limited lateral movement. Thus, for controlled levitation and rotation of cells with minimal stress due to the electrical forces, it is important to consider the contributions of the above mentioned electrical parameters. All cells used in the following experiments were cultured in RPMI-1640 growth medium (Gibco, Grand Island, NY) in 5% CO_2 and 37°C. The medium was supplemented with 10% fetal bovine serum, 2 mM L-glutamine, 100 µg /ml penicillin and 100 µg/ml streptomycin. Figure 35 shows a near spherical K-562 leukemia cancer cell being electrorotated using a flat head electrocage with interspacing 60µm. The rotation axis is in the plane of the figure running from top left to bottom right corner perpendicular to the direction of imaging. Note that the cell is levitated to the middle plane of the electrocage and therefore the electrodes are not in focus.

60
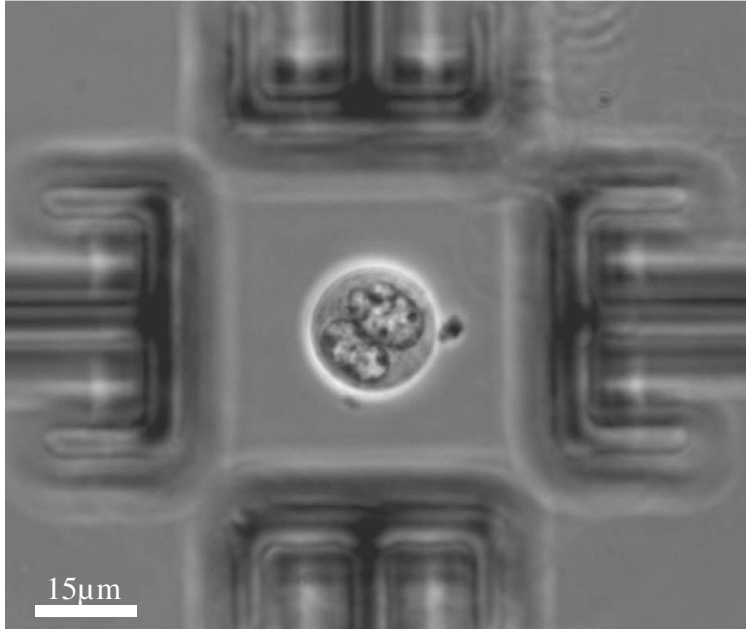
Figure 35. Image of K-562 cell electrorotation in ROT chip

4.1 Voltage characterization

Since the transmembrane potential and therefore the electrical stress on the cell increases with the applied voltage, it is necessary to minimize the applied potential at a given frequency while still maintaining the trap stability (Glasser and Fuhr 1998). However, to rotate cells in a stable manner, the applied voltage should be sufficient to levitate the trapped cell to the center of the electrocage. Operable voltages were determined experimentally for K-562 and Murine cells suspended in RPMI medium of conductivity 1.5 $\pm$ 0.2 S/m at 23 °C. Obviously, the levitation force is dependent on the type, size, shape and health (determines the permittivity and conductivity) of the cells. So, ten approximately spherical cells from each cell line were electrorotated in a 60µm spaced octupole ROT chip with flat electrodes to find the minimum operable voltage. The ROT chip was driven by the Highland T340 function generator at 2MHz with phase

configuration 1 shown in Table 2. The cells used were in good health, and had been incubated in a 37°C 5% CO_2 environment until at least 90 minutes before testing. The average size of K-562 cells were 17.7 $\pm$ 2.3µm (max - 21 µm, min - 14 µm) and Murine cells were 14.1$\pm$ 1.4 µm (max- 16 µm, min-12 µm). Videos and pictures of rotating cells at various voltages were acquired and the difference in levitation was determined visually.

Figure 36. Cumulative K-562 cell levitation versus excitation voltage amplitude
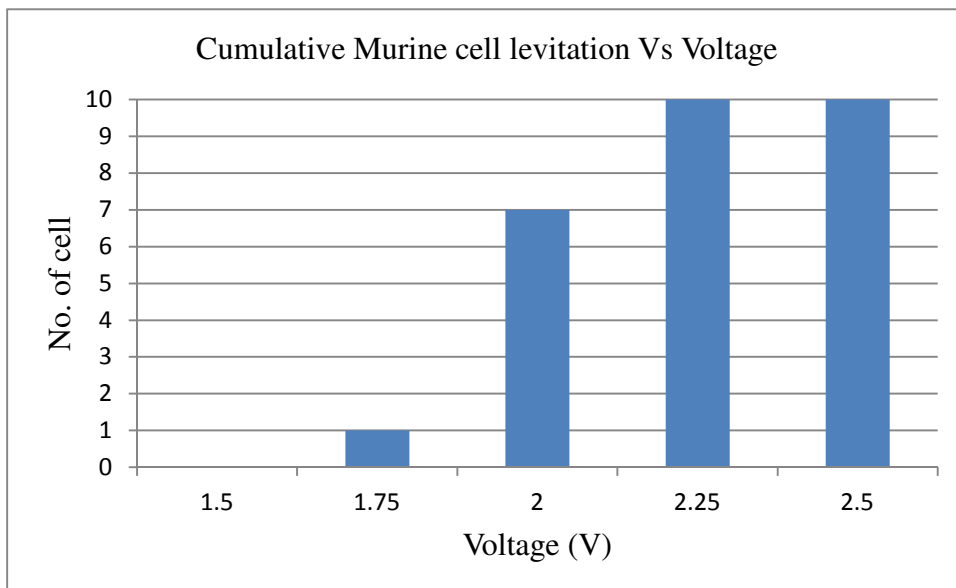
Figure 37. Cumulative Murine cell levitation versus excitation voltage amplitude
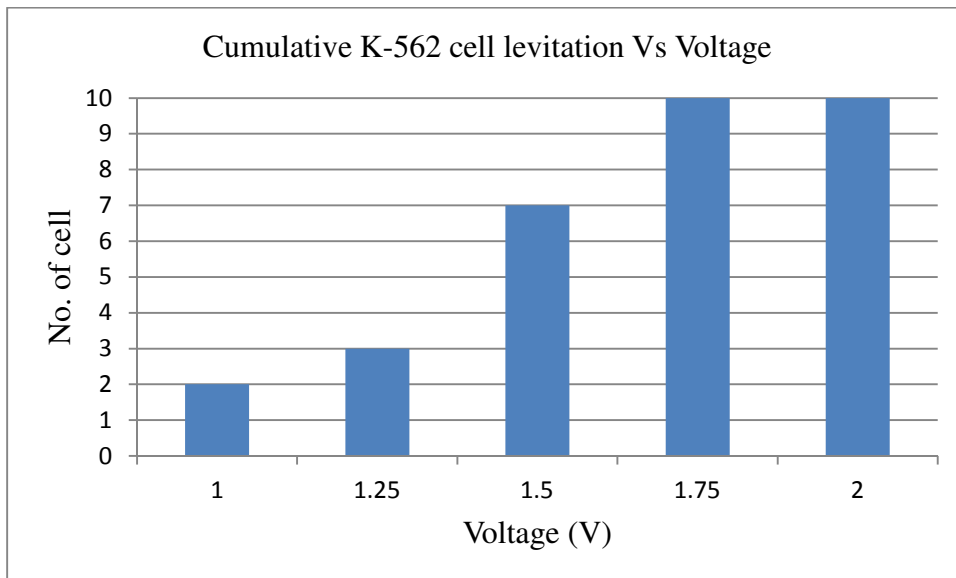
The column charts shown in Figures 36 and 37 shows the cumulative number of cells that were levitated to the center of the cage upon applying different voltages. For example, at 2.25 V, every Murine cell of the ten cells tested was levitated. Prior to each evaluation, every K-562 cell was rotated at 2V amplitude and every Murine cell was rotated at 2.5V to determine the plane for optimal levitation. Voltage was then reduced and levitation plane was determined in intervals of 0.25V until the maximum voltage (2V for K-562 and 2.5V for Murine) was reached. It can be seen from the column charts that 1.75V amplitude and 2.25V amplitude are safe operable voltages for K-562 and Murine cells respectively. These results hold for the given electrode type and spacing, the applied frequency, and the phase configuration.

4.2 Frequency characterization

The frequency dependence of the cell rotation is reflected by the Clausius-Mossotti factor. It is optimal to choose the frequency that will exert the maximum force for a given voltage to enhance the stability and also reduce the transmembrane potential of a cell (Muller et al. 1999). Therefore, optimal operation frequencies were determined for K-562, Murine cells and PolyMethylMethAcrylate (PMMA) 15 µm microbeads (Bangs laboratories Inc.) suspended in RPMI medium of conductivity 1.5 ± 0.2 S/m at 23 °C. A total of 10 near spherical cells in each cell line within 90 minutes from 37 °C, 5% CO_2 incubator and 10 microbeads were electrorotated in this experiment. The tested K-562 cells were 17.6 ± 2.4µm (max - 21 µm, min - 14 µm), the Murine cells were 14.6 ± 2.0 µm (max- 20 µm, min-12 µm) and the PMMA microbeads were

63

15.8±0.6µm. The microbeads were hemispherically coated in chromium so that their rotational rate could be determined. To do this, the microbeads were embedded in 7.5µm AZ4620 photoresist and deposited with 20nm of chromium using Edward-2 thermal evaporator. The photoresist was then removed and the beads were resuspended in the cell medium. The testing was done in an octupole flat head ROT chip with spacing 60µm. The electrodes were operated with phase configuration 1 that is shown in Table 2. The ROT chip was driven with 2V for K-562 cells, 2.25V for Murine cells and 2.5V for PMMA microbead by the NI PXI 1045 function generator. Videos and pictures of rotating cells/beads at different frequencies were acquired and the rotation rates were determined visually.
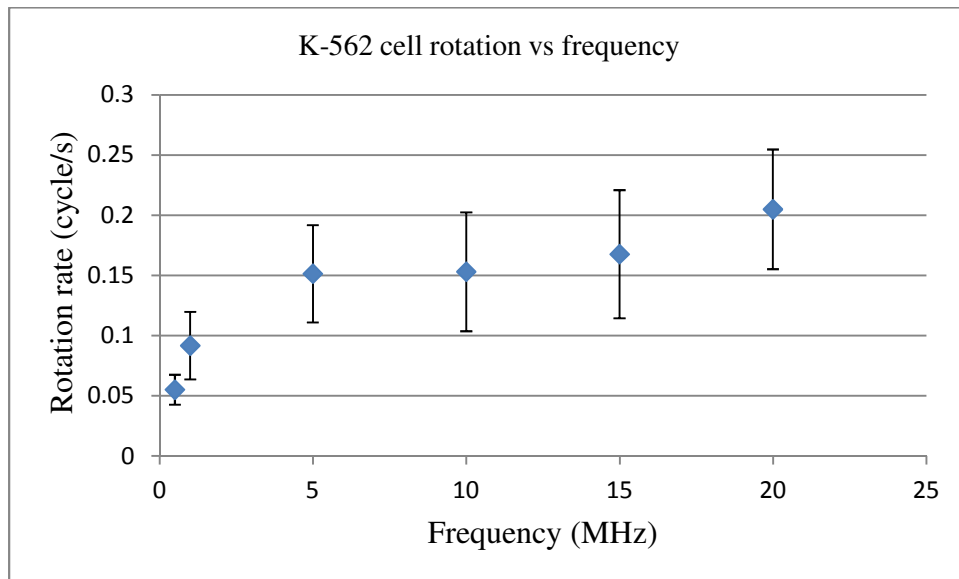
Figure 38. K-562 cell rotation rate versus excitation frequency
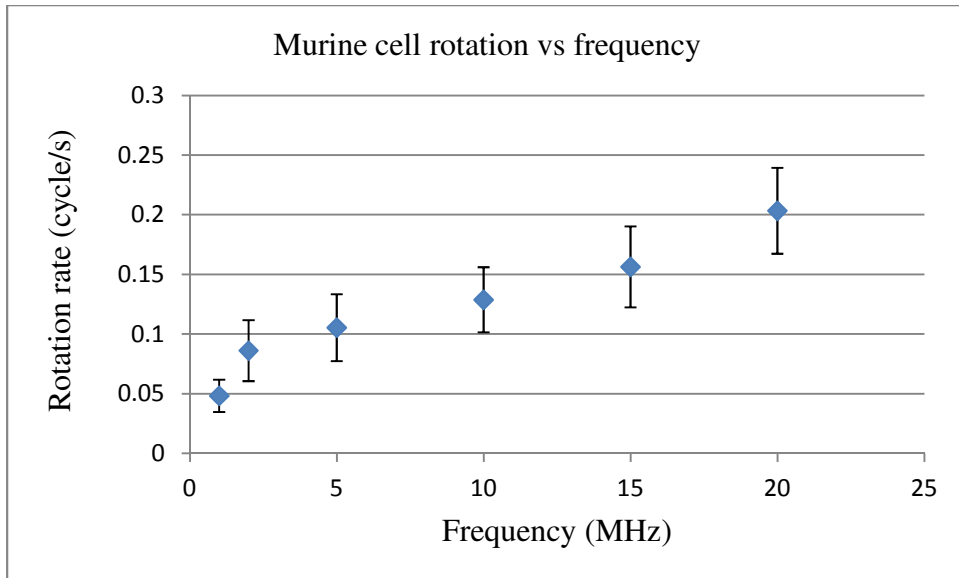
Figure 39. Murine cell rotation versus excitation frequency
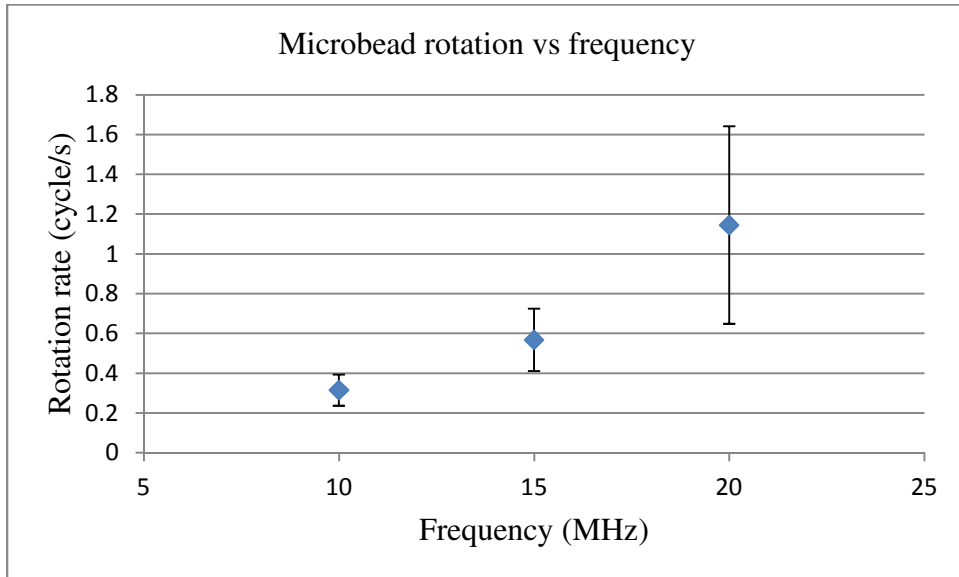
Figure 40. PMMA microbead rotation versus excitation frequency

In the Figures 38, 39 and 40 the rotation rates (in cycles/s) of K-562, Murine cells and microbead versus frequency have been plotted respectively. It can be seen that with increase in the frequency there is increase in the ROT and DEP forces and therefore the rotation rate for the fixed voltage values. The high SD in rotation rates of cells indicates the heterogeneity caused by variance in the

cell size, shape and the electrical properties of the cells (Clausius-Mossotti factor). In the case of the microbeads, the amount of deposited chromium was not controlled, leaving excess chromium particles anisotropically attached to the microbeads. Comparing the Clausius-Mossotti factor versus frequency plot in Section 2.2.3 to that of the rotation rates versus frequency, it can be observed that there is negative DEP force and slow rotation rates for the given value of medium conductivity 1.5S/m. However, the simplified cell model used in the Clausius-Mossotti plot does not completely explain the cell rotation behavior. The ROT torque continuously increases with increase in frequency. Therefore, the ideal frequency of operation should be as low as possible as very low rotation rates are desired. But, the limiting factors for low frequency operation are Joule heating and cell transmembrane potential. The transmembrane potential is minimal for frequency values more than 5MHz (Glasser and Fuhr 1998). Increase in transmembrane potential may result in quicker compromise of the cell membrane. However, in Section 4.6, cell rotation under low frequency ranges (500 kHz – 2MHz) has been performed for 60 minutes without significant damage to the cells. This implies that cell rotation under low frequencies (500 kHz – 2MHz) may suit for imaging purposes. Detailed studies on the effects due to applied electric fields should be carried out for quantitative determination of cell stress.

4.3 Cell size, shape and type

The DEP and ROT force have a cubic dependence on the radius of the cell assuming it to be spherical. Both the cell lines characterized are of similar size ranges. However, from the Figures in previous section, it can be seen that the

average rotation rate of the K-562 cells is slightly greater than that of the Murine cells despite using 2V for K-562 cells and 2.25V for Murine cells. An exclusive characterization of the rotation rate with respect to size was not performed to explore this behavior further.

4.4 Cell medium conductivity

The conductivity of the cell mediums were measured, whereas the other parameters (conductivity of cell, permittivity of cell and medium) were not determined as part of this project. In Table 8 below, the conductivity values of several commonly used media are listed.

Table 8. Cell medium conductivity values

Cell medium	Conductivity (S/m) @ 22.4°C
RPMI	1.36
DMEM	1.79
EMEM	1.67
Keratinocyte	1.57

4.5 Electrode shape, spacing and number

The electrode shape, spacing and number influence the electric field distribution inside the electrocage. The electrode shape and number have been simulated in COMSOL, and optimized for maximum electrorotation and trapping. The electrode spacing has dependence on the height of the microchannel for electric field symmetry. But, the height is limited by the distance the cell can be levitated from bottom substrate. The main constraint being the working distance

67

of the objectives used. Therefore, the electrode interspacing and height was fixed at 60µm.

4.6 Trypan blue cell rotation longevity characterization

As mentioned earlier, the electrical forces and Joule heating can have detrimental effects on the cell. Therefore, it is necessary to find the longevity of cell rotation using the electrocage. Cell cultivation/manipulation in presence of electric field has been extensively studied by Fuhr et al (Fuhr et al. 1994; Glasser and Fuhr 1998). It has been stated that at low frequencies (<1MHz) the field application is limited by the dielectric breakdown of cell membrane due to high transmembrane potential values while at high frequencies (>5MHz) much higher fields can be applied and Joule heating is the limitation factor.

Table 9. Trypan blue cell electrorotation longevity characterization

Cell	Voltage (V)	Frequency (MHz)	Viability
1	4	2	< 2 minutes
2	2	2	>60minutes
3	2	1	>60minutes
4	2	0.5	>60minutes

Cell rotation longevity was analyzed by using Trypan blue absorption dye. Trypan blue is an exclusion dye which stains only dead cells and does not permeate into live cells. This property can be useful in probing the viability of cells during and after cell rotation (Frenea et al. 2003). In this experiment, 100µl of trypan blue dye (T8154- 0.4%, Sigma Aldrich, St. Louis, MO) was added to 1ml of K-562 cells suspended in RPMI medium and flowed into the ROT chip. Flat head octupole ROT chip with interspacing 60µm was excited using T-340

function generator (maximum frequency – 2MHz). Four cells were tested with different voltages and frequencies as shown in the Table 9.

Even though the sample set in the experiment is less, it clearly indicates that at very high voltages ($\geq$ 4V) the cell membrane is compromised very soon (<2 min.). While at 2V, cells continuously rotated for an hour with no visible effect on the cell membrane as no trypan blue was observed in the cell cytoplasm. Also, after 1 hr rotation at 2V, applying 4V to 3 cells resulted in faster cell degradation (<1minute). Figure 41, shows cell 1 which was electrorotated with 4V and 2MHz at 0 min (left) and 2 min(right). Figure 42, shows cell 4 which was electrorotated with 2V and 500KHz at 0 min (left) and 60 min(right). Another important effect of DEP force on the cell that is evident from the figures even at low voltage is that after sufficient exposure to DEP forces, the cell becomes more spherical which can be attributed to the constant repelling force pushing the cell to the center of the electrocage. This effect can be reduced by decreasing the operation voltage without sacrificing levitation and avoiding long electrorotation times.
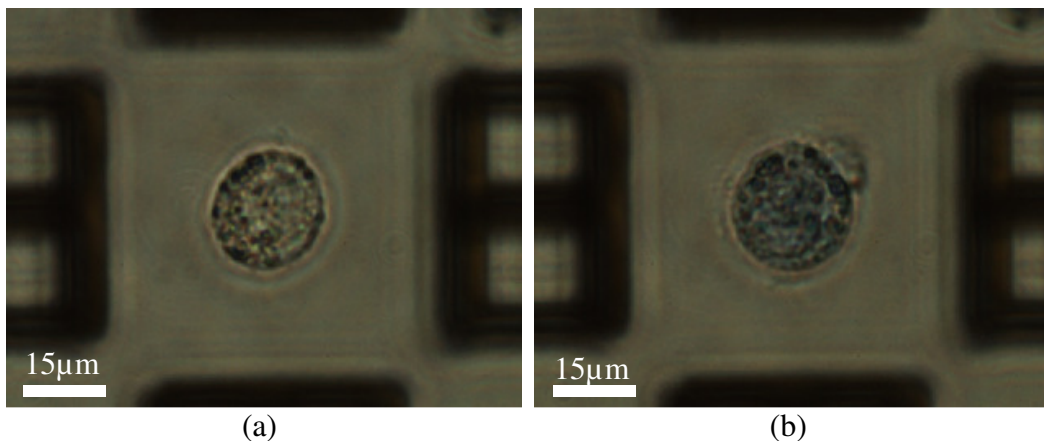

(a)   (b)

Figure 41. Image of K-562 cell before (a) and after (b) electrorotation at 4Vamplitude, 2MHz for 2 minutes

<div align="center">(a)   (b)</div>
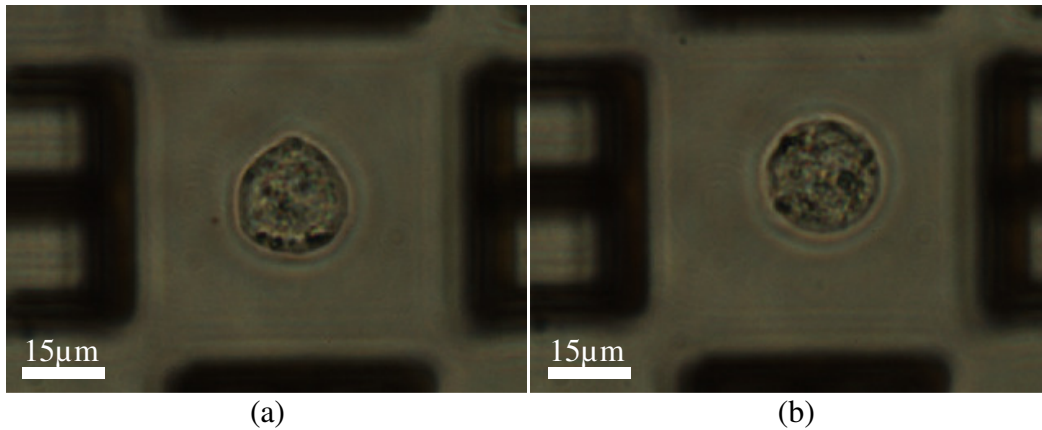
Figure 42. Image of K-562 cell before (a) and after (b) electrorotation at 2V amplitude, 500kHz for 60 minutes

4.7 Rhodamine-B characterization of Joule heating

Rhodamine B is a water-soluble dye that is commonly used for staining cells and as a tracer. It belongs to a class of fluorophores whose fluorescence intensities are highly dependent on temperature. And therefore, Rhodamine B allows for temperature measurements in microfluidic systems with good spatial and temporal resolution (Ross, Gaitan, and Locascio 2001).

The effect of Joule heating has been studied by Fuhr et al. (Glasser and Fuhr 1998). It has been shown that the temperature increase ($\Delta T \simeq 2.5°C$) remains almost constant with a constant electric field over a wide range of frequencies (100 KHz – 100MHz). But, for an applied voltage, the potential drop and therefore the electric field vary with frequency which depends on the electrical properties of the medium. However, in the preliminary tests reported here, the voltage is varied and electric field inside the ROT chip is not probed. In order to find the temperature gradients occurring inside the ROT chip in the electrocage region due to Joule heating, rhodamine dye dissolved in IMDM cell medium of conductivity 1.5 $\pm$ 0.2 S/m at 23°C was used. Octupole flat head ROT

chip with 60µm was used. The dye was flowed inside the electrocage and different voltage was applied. The resulting intensity of the dye was measured using a fluorescence microscope. The Nikon TE 2000E confocal microscope used a Xenon light source filtered to an excitation wavelength of 542-567nm and an emission wavelength of 579nm-631nm. In order to calibrate the temperature, the ROT chip with Rhodamine B dye in the microchannel was placed inside an on-stage incubator unit (INU series, Tokai Hit Co., Ltd) with predefined temperature settings and the fluorescence intensity was measured. As shown in Figure 44, the fluorescence intensity was obtained for various temperatures. The temperature inside the ROT chip was probed by averaging the measurements obtained using two thermocouples on the top and bottom of the ROT chip. Then the ROT chip was maintained at room temperature and driven using the Highland T340 function generator. 1-4 V amplitude with intervals of 1 V was applied to the electrodes with phase config 1 as shown in Table 2 and two different frequencies 500 KHz and 2 MHz (maximum). Two trials were recorded for each experiment and fresh IMDM medium was pumped to the cage after every experiment giving sufficient time for the residual flow to settle and for the intensity of the dye to equilibrate after applying a voltage. The average fluorescence intensity was calculated over the electrocage area (ROI) as shown in Figure 43 for various preset incubation temperatures and voltages applied.
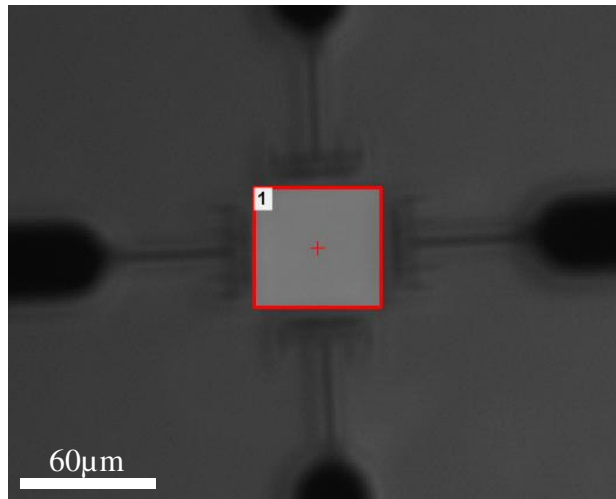
Figure 43. Region of interest used to evaluate the fluorescence intensity
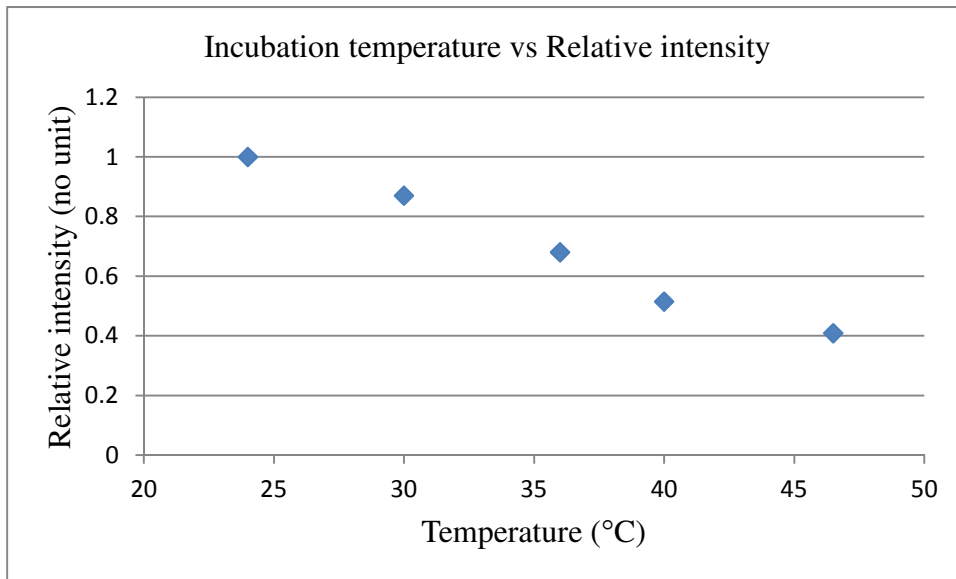
Figure 44. Incubation temperature versus relative fluorescence intensity
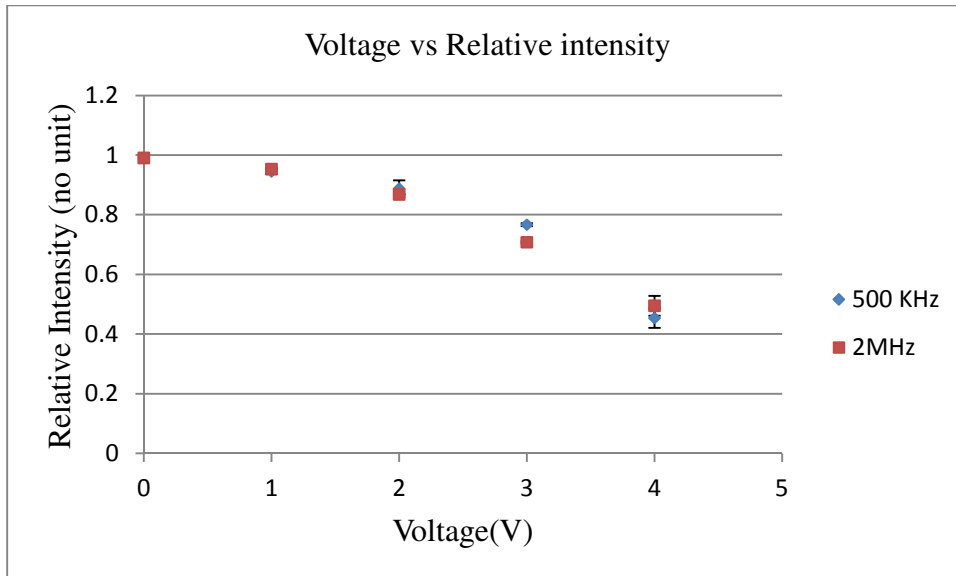
Figure 45. Excitation voltage versus relative fluorescence intensity

Figures 44 and 45, show the relative fluorescence intensity (with respect to RT $=23.85\pm 0.15°C$) of Rhodamine-B dye in the ROI. It can be seen that with the increase in the incubation temperature and voltage applied, the intensity of the dye reduces. In the voltage ranges of interest (~ 2V amplitude), from the calibration curve, it can be inferred that the temperature in the electrocage region increases by around 7 °C from RT. And at high voltages (~ 4V amplitude), the temperature in the electrocage is very high and definitely not a favorable condition for live cells. The fluorescence intensity doesn't seem to vary much for the frequency ranges considered. Therefore, to minimize the effect of Joule heating, voltage values below 2V for the given frequency range is optimal. The effect of Joule heating at high frequencies (~20MHz) can be much lower and therefore operation at high frequencies and lower voltages can be advantageous in reducing Joule heating.

4.8 Discussion

The dielectrophoretic responses of two different cell lines have been analyzed by varying the applied voltage and frequency. Comparing the simulation results to the experimental observations, the frequency response of the rotation rate of cells follows the similar trend as that of the Im (f_{CM}) for a fixed medium conductivity of 1.5 S/m. The main limiting factors for operable frequency are cell transmembrane potential (low frequency) and high rotation rates (high frequency). The voltage is limited by the levitation F_{DEP} force. Joule heating in the voltage and the frequency range of interest has been probed. Also, the longevity of cell electrorotation under the influence of electric fields has been measured. With the experimentally observed results, it can be concluded that precise electrorotation of cells is possible with the ROT chip for optical imaging purpose. The slowest rotation achieved with the ROT chip in an average is 0.05 cycles/s. It is desired to achieve much slower rotation which may be possible by tweaking the electrical or fluidic parameters of the cell medium in the voltage and frequency range of interest.

Chapter 5

Conclusion and future work

As presented in this thesis, a ROT chip has been developed which is capable of precise electrorotation of single cells in 3-D. Although, the chip design and fabrication protocol have been specifically developed for cell rotation, the principles of DEP can be used to easily develop additional functional structures which can perform other functions like funneling, concentrating, parking(http://www.youtube.com/watch?v=_nJCLxbiiNs&context=C433c6a5AD vjVQa1PpcFMvMpoVA6Jdw4-lUaAdww6_ZEY9fSv9OeI=) and separating, thus offering additional functionality to the chip (Muller et al. 1999). Many can be integrated into the chip to make the chip more versatile and eventually a true "lab-on-chip". In this thesis, only prevalently used electrode designs and fabrication techniques have been analyzed, focusing specifically on electrorotation Also, it has been shown that the electric field distribution in an electrocage varied minimally across various electrode shapes (Schnelle, Muller, and Fuhr 2000). Therefore, further modifications to the electrode head shape may not offer huge improvements in performances.

Considering the design, the current electrode shapes (flat, semi-elliptical and arrow) is more than sufficient to deliver precise rotation of cells. It can be advantageous to modify the electrode design to reduce thermal convection, to improve fabrication yield, or to repel cells on the outside of the electrocage. Also, additional functional structures to aid in cell delivery and retrieval can be designed as mentioned before.

Regarding the fabrication protocol of the ROT chip, the process steps have been optimized for repeatable fabrication with minimal tolerances. However, only 500 µm thick glass wafers have been used for fabrication, which is much thicker than the 170 µm thick glass required for high magnification imaging. Fabrication and integration of features with wafers as thin as 170 µm may be a significant challenge as handling can be risky. Because ROT chip requires fluidic and electric connections, holes must be cut in the wafers before being bonded. In this step, the wafers are vulnerable to breakage during extraction from the machining substrate. Bonding poses the greatest risk of breakage in the fabrication process; however, diffusive bonding allows for the use of relatively low pressures to bond the chip halves when compared to the bonder tool (which exerts ~ 2kN). The diffusive bonding technique must be optimized for wafer level bonding. To overcome the difficulties of handling and transporting the wafers between processes, supportive holders can be used (for example, a 500 µm thick wafer stuck under the 170 µm during fabrication process). Fabrication could also be done on a 500 µm thick wafer that would then be etched down to 170 µm with hydrofluoric acid/Buffered Oxide Etchant (BOE). In any case, the durability of the ROT chip itself with 170 µm glass will be lower than with 500 µm glass. A 500 µm top substrate and 170 µm bottom substrate, can also be used on an inverted microscope assuming that this does not introduce any new challenges for imaging.

Another challenge with the current fabrication process is its low throughput. The main constraints lie in the large form factor of each chip (design

iteration 2.0 – 1" * 2.5"), the gold deposition tool (Edwards-2 thermal evaporator), and the diffusive bonding process. As clearly stated in Table 3, the Edwards-2 thermal evaporator offers a more durable and defect free gold layer. However, its low throughput (1 wafer at a time) and high material expenses make it unattractive. The diffusive bonding process has to be done on a chip basis, limiting throughput. Although it would be more efficient, the inherent non-uniformity of the photoresist layer poses a major challenge for wafer level bonding with the EVG 520 bonder as shown in Figure 29.

With the acquired cell electrorotation characterization data, it is possible to deduce the trend that can be expected with any future experiments. A good understanding of the electrokinetic principles that govern the ROT chip operation is very important for future developments. The current imaging capabilities require that the cell rotation rate be as low as one rotation every minute. However, the slowest rotation rate achieved with the threshold voltages mentioned in Section 4.1 is roughly 0.05cycles/s (20s per rotation). This implies that new techniques to reduce the rotation rate must be developed. Possible work around could be to use a combination of optical trapping and DEP to rotate cells at lower voltages and therefore slower or increase the viscosity of the cell medium without affecting the electrical properties of the medium so that the opposing viscous drag force reduce the rotation rate. Changing the conductivity of the medium might be a possibility considering the Clausius-Mossotti factor behavior, but it is of great interest not to alter the constituents of the cell medium to keep the cell viability high.

Other challenges to be solved with the ROT chip are to reduce Joule heating due to applied electric fields and to probe the effects of electric field on the viability of cells. It has been shown by Fuhr et al that cells can be cultured in presence of high AC electric fields under similar conditions used in the ROT chip (Fuhr et al. 1994). However, considering the observations in the Rhodamine-B Joule heating test and Trypan blue cell rotation longevity test, it is necessary to probe the effect of electric fields on the cell in greater detail.

One drawback of the ROT chip is that precise uniaxial electrorotation of non-spherical cells can be difficult. The cell positions itself to minimize the DEP force acting on it and this could lead to multiaxial rotation (if the cell is significantly non-spherical). Also, so far, only non-adherent cells have been electrorotated. Electrorotation of adherent cells will be possible only by typsinizing the cells so they are in suspended state.

REFERENCES

Abgrall, P., V. Conedera, H. Camon, A. M. Gue, and N. T. Nguyen. 2007. SU-8 as a structural material for labs-on-chips and microelectromechanical systems. *Electrophoresis* 28 (24):4539-4551.

An, J., J. Lee, S. H. Lee, J. Park, and B. Kim. 2009. Separation of malignant human breast cancer epithelial cells from healthy epithelial cells using an advanced dielectrophoresis-activated cell sorter (DACS). *Analytical and Bioanalytical Chemistry* 394 (3):801-809.

Andersson, H., and A. van den Berg. 2003. Microfluidic devices for cellomics: a review. *Sensors and Actuators B-Chemical* 92 (3):315-325.

Arnold, W. M., and U. Zimmermann. 1988. Electro-rotation - development of a technique for dielectric measurements on individual cells and particles. *Journal of Electrostatics* 21 (2-3):151-191.

Chollet, F. SU-8: Thick Photo-Resist for MEMS,memscyclopedia.org. 2009. Available from http://memscyclopedia.org/su8.html.

Cui, L., and H. Morgan. 2000. Design and fabrication of travelling wave dielectrophoresis structures. *Journal of Micromechanics and Microengineering* 10 (1):72-79.

Djuzenova, C. S., U. Zimmermann, H. Frank, V. L. Sukhorukov, E. Richter, and G. Fuhr. 1996. Effect of medium conductivity and composition on the uptake of propidium iodide into electropermeabilized myeloma cells. *Biochimica Et Biophysica Acta-Biomembranes* 1284 (2):143-152.

Fiedler, S., S. G. Shirley, T. Schnelle, and G. Fuhr. 1998. Dielectrophoretic sorting of particles and cells in a microsystem. *Analytical Chemistry* 70 (9):1909-1915.

Frenea, M., S. P. Faure, B. Le Pioufle, P. Coquet, and H. Fujita. 2003. Positioning living cells on a high-density electrode array by negative dielectrophoresis. *Materials Science & Engineering C-Biomimetic and Supramolecular Systems* 23 (5):597-603.

Fuhr, G., H. Glasser, T. Muller, and T. Schnelle. 1994. Cell manipulation and cultivation under AC electric-field influence in highly conductive culture media. *Biochimica Et Biophysica Acta-General Subjects* 1201 (3):353-360.

Fuhr, G., and P. I. Kuzmin. 1986. Behavior of cells in rotating electric-fields with account to surface-charges and cell structures. *Biophysical Journal* 50 (5):789-795.

Fuhr, G., T. Schnelle, S. Fiedler, and S.G Shirley. 2003. Electrode array for field cages. USA. US 6610188 B1. Aug 26, 2003

Glasser, H., and G. Fuhr. 1998. Cultivation of cells under strong ac-electric field - differentiation between heating and trans-membrane potential effects. *Bioelectrochemistry and Bioenergetics* 47 (2):301-310.

Green, N. G., and H. Morgan. 1997. Dielectrophoretic separation of nano-particles. *Journal of Physics D-Applied Physics* 30 (11):L41-L44.

Heida, Tjitske. 2003. *Electric field-induced effects on neuronal cell biology acompanying dielectrophoretic trapping*. Germany: Springer-Verlag Berlin Heidelberg.

Jones, Thomas B. 1995. *Electromechanics of particles*. New York: Cambridge University Press.

Juang, J.L, Y.Y Huang, and P.C Chen. 2010. Microarray chip and method of fabricating for the same.USA. US 2010/0167950 A1. Dec 30, 2009

Lapizco-Encinas, B. H., B. A. Simmons, E. B. Cummings, and Y. Fintschenko. 2004. Dielectrophoretic concentration and separation of live and dead bacteria in an array of insulators. *Analytical Chemistry* 76 (6):1571-1579.

Repeated Author. 2004. Insulator-based dielectrophoresis for the selective concentration and separation of live bacteria in water. *Electrophoresis* 25 (10-11):1695-1704.

Maswiwat, K., M. Holtappels, and J. Gimsa. 2006. On the field distribution in electrorotation chambers - Influence of electrode shape. *Electrochimica Acta* 51 (24):5215-5220.

Morgan, H., N. G. Green, M. P. Hughes, W. Monaghan, and T. C. Tan. 1997. Large-area travelling-wave dielectrophoresis particle separator. *Journal of Micromechanics and Microengineering* 7 (2):65-70.

Muller, T., G. Gradl, S. Howitz, S. Shirley, T. Schnelle, and G. Fuhr. 1999. A 3-D microelectrode system for handling and caging single cells and particles. *Biosensors & Bioelectronics* 14 (3):247-256.

Nandakumar, V., L. Kelbauskas, R. Johnson, and D. Meldrum. 2011. Quantitative Characterization of Preneoplastic Progression Using Single-Cell

Computed Tomography and Three-Dimensional Karyometry. *Cytometry Part A* 79A (1):25-34.

Niklaus, F., P. Enoksson, E. Kalvesten, and G. Stemme. 2003. A method to maintain wafer alignment precision during adhesive wafer bonding. *Sensors and Actuators a-Physical* 107 (3):273-278.

Niklaus, F., G. Stemme, J. Q. Lu, and R. J. Gutmann. 2006. Adhesive wafer bonding. *Journal of Applied Physics* 99 (3).

Nilsson, J., M. Evander, B. Hammarstrom, and T. Laurell. 2009. Review of cell and particle trapping in microfluidic systems. *Analytica Chimica Acta* 649 (2):141-157.

Oh, J., R. Hart, J. Capurro, and H. Noh. 2009. Comprehensive analysis of particle motion under non-uniform AC electric fields in a microchannel. *Lab on a Chip* 9 (1):62-78.

Ray, T, *H Zhu*, and *I.S* El*ango*. 2011. Characterization of KMPR$^{®}$1025 as a masking layer for deep reactive ion etching of fused silica. Paper read at MEMS IEEE 24th conf.

Reichle, C., T. Muller, T. Schnelle, and G. Fuhr. 1999. Electro-rotation in octupole micro cages. *Journal of Physics D-Applied Physics* 32 (16):2128-2135.

Ross, D., M. Gaitan, and L. E. Locascio. 2001. Temperature measurement in microfluidic systems using a temperature-dependent fluorescent dye. *Analytical Chemistry* 73 (17):4117-4123.

Schnelle, T., R. Hagedorn, G. Fuhr, S. Fiedler, and T. Muller. 1993. 3-Dimensional electric-field traps for manipulation of cells - calculation and experimental- verification. *Biochimica Et Biophysica Acta* 1157 (2):127-140.

Schnelle, T., T. Muller, S. Fiedler, and G. Fuhr. 1999. The influence of higher moments on particle behaviour in dielectrophoretic field cages. *Journal of Electrostatics* 46 (1):13-28.

Schnelle, T., T. Muller, and G. Fuhr. 2000. Trapping in AC octode field cages. *Journal of Electrostatics* 50 (1):17-29.

Schnelle, T., T. Muller, C. Reichle, and G. Fuhr. 2000. Combined dielectrophoretic field cages and laser tweezers for electrorotation. *Applied Physics B-Lasers and Optics* 70 (2):267-274.

Sebastian, A., A. M. Buckle, and G. H. Markx. 2006. Formation of multilayer aggregates of mammalian cells by dielectrophoresis. *Journal of Micromechanics and Microengineering* 16 (9):1769-1777.

Serra, S.G., A Schneider, K Malecki, Huq.S.E, and Brenner.W. 2007. A simple bonding process of SU-8 to glass to seal a microfluidic chip.

Shafiee, Hadi, John L. Caldwell, Michael B. Sano, and Rafael V. Davalos. 2009. Contactless dielectrophoresis: a new technique for cell manipulation. *Biomedical Microdevices* 11 (5):997-1006.

Sung, J.M. 2007. Dielectrophoresis and Optoelectronic Tweezers for Nanomanipulation.

Taff, B. M., and J. Voldman. 2005. A scalable addressable positive-dielectrophoretic cell-sorting array. *Analytical Chemistry* 77 (24):7976-7983.

Voldman, J. 2006. Electrical forces for microscale cell manipulation. *Annual Review of Biomedical Engineering* 8:425-454.

Wang, D. J., and S. Bodovitz. 2010. Single cell analysis: the new frontier in 'omics'. *Trends in Biotechnology* 28 (6):281-290.

Washizu, M., and T. B. Jones. 1994. 3-Dimensional electric-field traps for manipulation of cells - calculation and experimental- verification. *Journal of Electrostatics* 33 (2):187-198.

Zahn, Jeffrey D. 2009. *Methods of Bioengineering: Biomicrofabrication and biomicrofluidics*. Norwood,USA: Artech House.